

# Redox Non-innocence of Thioether Crowns: Elucidation of the Electronic Structure of the Mononuclear Pd(III) Complexes [Pd([9]aneS<sub>3</sub>)<sub>2</sub>]<sup>3+</sup> and [Pd([18]aneS<sub>6</sub>)]<sup>3+</sup>

Emma Stephen,<sup>†</sup> Alexander J. Blake,<sup>†</sup> Emma Carter,<sup>‡</sup> David Collison,<sup>§</sup> E. Stephen Davies, Ruth Edge,<sup>§</sup> William Lewis,<sup>†</sup> Damien M. Murphy,<sup>‡</sup> Claire Wilson,<sup>†</sup> Robert O. Gould,<sup>⊥</sup> Alan J. Holder,<sup>⊥</sup> Jonathan McMaster,<sup>\*,†</sup> and Martin Schröder<sup>\*,†</sup>

<sup>†</sup>School of Chemistry, University of Nottingham, Nottingham, NG7 2RD, U.K.

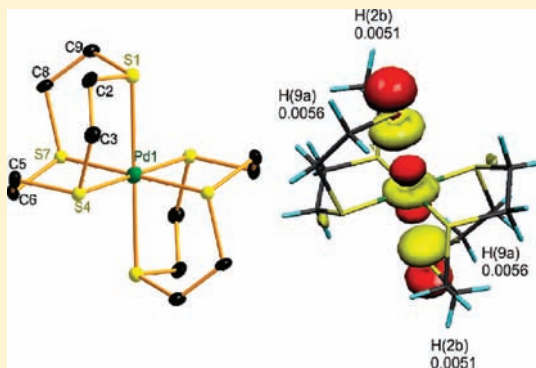
<sup>‡</sup>School of Chemistry, Cardiff University, Cardiff, CF10 3AT, U.K.

<sup>§</sup>EPSRC Multi-Frequency EPR Centre, School of Chemistry, University of Manchester, Manchester, M13 9PL, U.K.

<sup>⊥</sup>School of Chemistry, University of Edinburgh, Edinburgh, EH9 3JJ, U.K.

## Supporting Information

**ABSTRACT:** The Pd(II) complexes [Pd([9]aneS<sub>3</sub>)<sub>2</sub>](PF<sub>6</sub>)<sub>2</sub>·2MeCN (1) ([9]aneS<sub>3</sub> = 1,4,7-trithiacyclononane) and [Pd([18]aneS<sub>6</sub>)](PF<sub>6</sub>)<sub>2</sub> (2) ([18]aneS<sub>6</sub> = 1,4,7,10,13,16-hexathiacyclooctadecane) can be oxidized electrochemically or chemically oxidized with 70% HClO<sub>4</sub> to [Pd([9]aneS<sub>3</sub>)<sub>2</sub>]<sup>3+</sup> and [Pd([18]aneS<sub>6</sub>)]<sup>3+</sup>, respectively. These centers have been characterized by single crystal X-ray diffraction, and by UV/vis and multifrequency electron paramagnetic resonance (EPR) spectroscopies. The single crystal X-ray structures of [Pd<sup>III</sup>([9]aneS<sub>3</sub>)<sub>2</sub>](ClO<sub>4</sub>)<sub>6</sub>·(H<sub>3</sub>O)<sub>3</sub>·(H<sub>2</sub>O)<sub>4</sub> (3) at 150 K and [Pd([18]aneS<sub>6</sub>)](ClO<sub>4</sub>)<sub>6</sub>·(H<sub>3</sub>O)<sub>3</sub> (4) at 90 K reveal distorted octahedral geometries with Pd–S distances of 2.3695(8), 2.3692(8), 2.5356(9) and 2.3490(6), 2.3454(5), 2.5474(6) Å, respectively, consistent with Jahn–Teller distortion at a low-spin d<sup>7</sup> Pd(III) center. The Pd(II) compound [Pd([9]aneS<sub>3</sub>)<sub>2</sub>](PF<sub>6</sub>)<sub>2</sub> shows a one-electron oxidation process in MeCN (0.2 M NBu<sub>4</sub>PF<sub>6</sub>, 293 K) at E<sub>1/2</sub> = +0.57 V vs. Fc<sup>+</sup>/Fc assigned to a formal Pd(III)/Pd(II) couple. Multifrequency (Q-, X-, S-, and L-band) EPR spectroscopic analysis of [Pd([9]aneS<sub>3</sub>)<sub>2</sub>]<sup>3+</sup> and [Pd([18]aneS<sub>6</sub>)]<sup>3+</sup> gives g<sub>iso</sub> = 2.024, |A<sub>iso</sub>(Pd)| = 18.9 × 10<sup>-4</sup> cm<sup>-1</sup>; g<sub>xx</sub> = 2.046, g<sub>yy</sub> = 2.041, g<sub>zz</sub> = 2.004; |A<sub>xx</sub>(Pd)| = 24 × 10<sup>-4</sup> cm<sup>-1</sup>, |A<sub>yy</sub>(Pd)| = 22 × 10<sup>-4</sup> cm<sup>-1</sup>, |A<sub>zz</sub>(Pd)| = 14 × 10<sup>-4</sup> cm<sup>-1</sup>, |a<sub>xx</sub>(H)| = 4 × 10<sup>-4</sup> cm<sup>-1</sup>, |a<sub>yy</sub>(H)| = 5 × 10<sup>-4</sup> cm<sup>-1</sup>, |a<sub>zz</sub>(H)| = 5.5 × 10<sup>-4</sup> cm<sup>-1</sup> for [Pd([9]aneS<sub>3</sub>)<sub>2</sub>]<sup>3+</sup>, and g<sub>iso</sub> = 2.015, |A<sub>iso</sub>(Pd)| = 18.8 × 10<sup>-4</sup> cm<sup>-1</sup>; g<sub>xx</sub> = 2.048, g<sub>yy</sub> = 2.036, g<sub>zz</sub> = 1.998; |a<sub>xx</sub>(H)| = 5, |a<sub>yy</sub>(H)| = 5, |a<sub>zz</sub>(H)| = 6 × 10<sup>-4</sup> cm<sup>-1</sup>; |A<sub>xx</sub>(Pd)| = 23 × 10<sup>-4</sup> cm<sup>-1</sup>, |A<sub>yy</sub>(Pd)| = 22 × 10<sup>-4</sup> cm<sup>-1</sup>, |A<sub>zz</sub>(Pd)| = 4 × 10<sup>-4</sup> cm<sup>-1</sup> for [Pd([18]aneS<sub>6</sub>)]<sup>3+</sup>. Both [Pd([9]aneS<sub>3</sub>)<sub>2</sub>]<sup>3+</sup> and [Pd([18]aneS<sub>6</sub>)]<sup>3+</sup> exhibit five-line superhyperfine splitting in the g<sub>zz</sub> region in their frozen solution EPR spectra. Double resonance spectroscopic measurements, supported by density functional theory (DFT) calculations, permit assignment of this superhyperfine to through-bond coupling involving four <sup>1</sup>H centers of the macrocyclic ring. Analysis of the spin Hamiltonian parameters for the singly occupied molecular orbital (SOMO) in these complexes gives about 20.4% and 25% Pd character in [Pd([9]aneS<sub>3</sub>)<sub>2</sub>]<sup>3+</sup> and [Pd([18]aneS<sub>6</sub>)]<sup>3+</sup>, respectively, consistent with the compositions calculated from scalar relativistic DFT calculations.



## INTRODUCTION

Although the chemistry of palladium complexes in the oxidation states 0, +1, +2, and +4 is well represented and understood, well-characterized compounds containing mononuclear Pd(III) centers remain relatively rare. Pd(III) species are often proposed or regarded as reactive intermediates, and are seldom isolated.<sup>1</sup> Binuclear species such as [Pd<sub>2</sub>(hpp)<sub>4</sub>Cl<sub>2</sub>] (hpp<sup>-</sup> = 1,3,4,6,7,8-hexahydro-2H-pyrimido[1,2-a]pyrimidine anion),<sup>2</sup> [Pd<sub>2</sub>(hpp)<sub>4</sub>(OBz)<sub>2</sub>]<sup>3</sup> and *cis*-[Pd<sub>2</sub>(C<sub>6</sub>H<sub>4</sub>PPh<sub>2</sub>)<sub>2</sub>(O<sub>2</sub>CR)<sub>2</sub>Cl<sub>2</sub>] (R = CH<sub>3</sub>, CF<sub>3</sub>, and CMe<sub>3</sub>)<sup>4</sup> containing formal Pd(III)–Pd(III) bonds have been isolated and characterized and, together with [Pd(bhq)Cl(OAc)]<sub>2</sub>

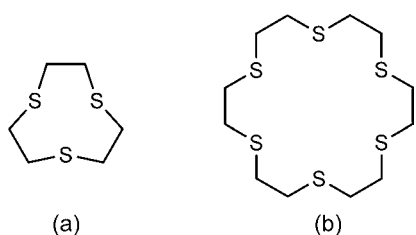
(bhq<sup>-</sup> = benzo[*h*]quinoliny),<sup>5</sup> these complexes show potential as catalysts in organic syntheses.<sup>6</sup> Recent work has described the syntheses and isolation of a series of halogen-bridged binuclear Pd(III)–Pd(III) species derived from the parent Pd(II) complexes [(L)Pd<sup>II</sup>X<sub>2</sub>] (X = Cl, Br; L = triaza macrocyclic ligands). These compounds have been proposed to catalyze Kharasch addition reactions.<sup>7a</sup> Related binuclear species have also been reported, the preparation of which can be achieved via the conversion of halogen-bridged

Received: August 4, 2011

Published: January 25, 2012

$-X\cdots M^{II}\cdots X-M^{IV}-X\cdots$  complexes to give  $-X-M^{III}-X-M^{III}-X-$  species ( $M = Pd$  and  $Pt$ ).<sup>7b</sup> Monomeric complexes of Pd(III) are rare, and  $[Pd^{III}(N_4)LL]^+$  ( $N_4 = N,N'$ -di-*tert*-butyl-2,11-diaza[3.3](2,6)pyridinophane),  $L = L' = CH_3$ ;  $L = C_6H_5$ ,  $L = CH_3$ ;  $L = CH_3$ ,  $L' = Cl$ ) can be prepared electrochemically or chemically from solutions of the parent Pd(II) complexes. Irradiation of these Pd(III) species results in C–C bond formation with ethane produced from the monomethyl complexes.<sup>8</sup>  $[PdF_6]^{3-}$  has been proposed to contain Pd(III) centers,<sup>9,10</sup> but is better formulated as  $Pd^{II}[Pd^{IV}F_6]^{2-}$ ,<sup>11,12</sup> while the anions  $[PdF_4]^-$ , and  $[PdF_6]^{3-}$  have been synthesized subsequently using solid-state methods.<sup>13–15</sup> The syntheses of aza- and thia-crown ether complexes  $[Pd([9]aneN_3)_2]^{3+}$  ( $[9]aneN_3 = 1,4,7$ -triazacyclononane)<sup>16</sup> and  $[Pd([9]aneS_3)_2]^{3+}$  ( $[9]aneS_3 = 1,4,7$ -trithiacyclononane, Scheme 1) containing

Scheme 1. Views of Ligands (a)  $[9]aneS_3$  and (b)  $[18]aneS_6$



Pd(III) centers have also been reported.<sup>17</sup> We have shown previously that macrocyclic ligands that incorporate homoleptic  $S_6$  thioether co-ordination can stabilize complexes containing late transition metal centers in unusual oxidation states.

Examples include Ni(III) in  $[Ni([9]aneS_3)_2]^{3+}$ ,<sup>18</sup> Pt(III) in  $[Pt([9]aneS_3)_2]^{3+}$ ,<sup>19,20</sup> Au(II) in  $[Au([9]aneS_3)_2]^{2+}$ , and Ag(II) in  $[Ag([18]aneS_6)]^{2+}$ .<sup>21</sup> We report herein the synthesis and structural, spectroscopic, electrochemical, and theoretical studies of the formally  $d^7$  Pd(III) complexes  $[Pd([9]aneS_3)_2]^{3+}$  and  $[Pd([18]aneS_6)]^{3+}$  ( $[18]aneS_6 = 1,4,7,10,13,16$ -hexathia-cyclooctadecane, Scheme 1). These studies represent the first comprehensive study of these centers and allows direct comparisons of their electronic structures with  $[Ni([9]aneS_3)_2]^{3+18}$  and  $[Pt([9]aneS_3)_2]^{3+19,20}$  analogues.

## RESULTS AND DISCUSSION

**Synthesis of  $[Pd([9]aneS_3)_2]^{2+/3+}$  and  $[Pd([18]aneS_6)]^{2+/3+}$ .** The macrocyclic ligands  $[9]aneS_3$  and  $[18]aneS_6$  were synthesized using reported literature methods.<sup>22</sup> The reaction of  $[9]aneS_3$  or  $[18]aneS_6$  with  $PdCl_2$  in  $MeOH/H_2O$  at reflux, followed by the addition of  $NH_4PF_6$ , yielded  $[Pd([9]aneS_3)_2](PF_6)_2$ <sup>17</sup> (1) or  $[Pd([18]aneS_6)](PF_6)_2$  (2) as blue-green solids. The electrochemical oxidation of  $[Pd([9]aneS_3)_2](PF_6)_2$  in  $MeCN$  (0.2 M  $NBu_4PF_6$ ) and the chemical oxidation of  $[Pd([9]aneS_3)_2](PF_6)_2$  and  $[Pd([18]aneS_6)](PF_6)_2$  in 70%  $HClO_4$  gave the corresponding formal air-stable Pd(III) products which were characterized by multifrequency and pulsed electron paramagnetic resonance (EPR) spectroscopies. Single crystals of  $[Pd([9]aneS_3)_2](ClO_4)_6 \cdot (H_2O)_3 \cdot (H_2O)_4$  (3) and  $[Pd([18]aneS_6)](ClO_4)_6 \cdot (H_2O)_2_3$  (4) suitable for X-ray crystallography were obtained by the reaction of  $[Pd([9]aneS_3)_2](PF_6)_2$  and  $[Pd([18]aneS_6)](PF_6)_2$ , respectively, with 70%  $HClO_4$  solutions at  $-20$  °C over one week.  $[Pd([9]aneS_3)_2]^{3+}$  and

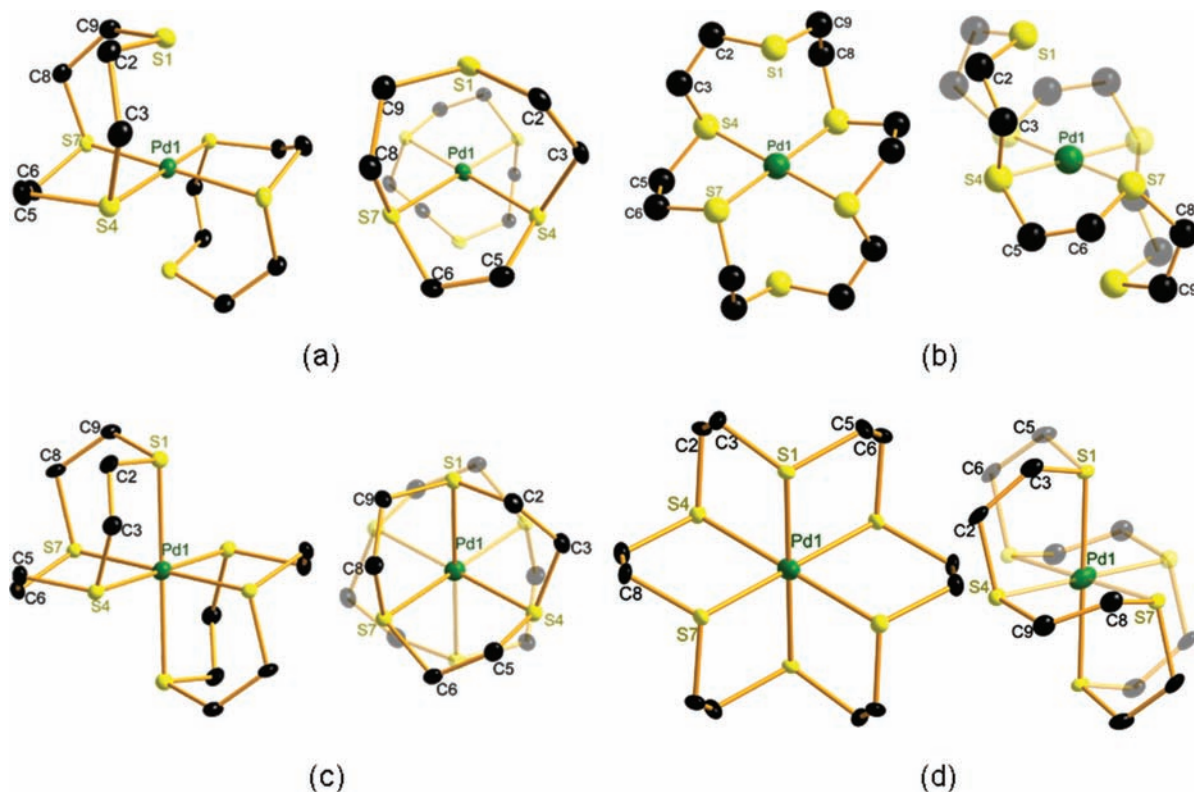


Figure 1. Views of (a)  $[Pd([9]aneS_3)_2]^{2+}$  in  $[Pd([9]aneS_3)_2](PF_6)_2 \cdot 2MeCN$ , (b)  $[Pd([18]aneS_6)]^{2+}$  in  $[Pd([18]aneS_6)](BPh_4)_2$ ; (c)  $[Pd([9]aneS_3)_2]^{3+}$  in  $[Pd([9]aneS_3)_2](ClO_4)_6 \cdot (H_2O)_3 \cdot (H_2O)_4$ , and (d)  $[Pd([18]aneS_6)]^{3+}$  in  $[Pd([18]aneS_6)](ClO_4)_6 \cdot (H_2O)_2_3$  showing the atom numbering scheme and 50% probability level displacement ellipsoids. Hydrogen atoms are omitted for clarity.

$[\text{Pd}([\text{18}] \text{aneS}_6)]^{3+}$  are stable in aerobic  $\text{HClO}_4$  solutions at this temperature for several months.

**Crystal Structures of  $[\text{Pd}([\text{9}] \text{aneS}_3)_2]^{2+/3+}$  and  $[\text{Pd}([\text{18}] \text{aneS}_6)]^{2+/3+}$ .** Single crystals of  $[\text{Pd}([\text{9}] \text{aneS}_3)_2](\text{PF}_6)_2 \cdot 2\text{MeCN}$  (**1**) were grown as dark blue blocky crystals by the diffusion of  $\text{Et}_2\text{O}$  vapor into a solution of  $[\text{Pd}([\text{9}] \text{aneS}_3)_2](\text{PF}_6)_2$  in MeCN. The structure of the  $[\text{Pd}([\text{9}] \text{aneS}_3)_2]^{2+}$  cation in  $[\text{Pd}([\text{9}] \text{aneS}_3)_2](\text{PF}_6)_2 \cdot 2\text{MeCN}$  (Figure 1a) shows that the Pd(II) ion is located at a crystallographic inversion center and is coordinated by two S-donor atoms in the equatorial plane derived from each of the two tridentate  $[\text{9}] \text{aneS}_3$  macrocyclic ring ligands in an approximate square planar geometry [Pd–S4 = 2.3195(7) and Pd–S7 = 2.3084(7) Å] (Table 1). Two S-donors occupy the axial positions and are located 2.9646(8) Å from the Pd<sup>II</sup> center.

The co-ordination sphere in  $[\text{Pd}([\text{9}] \text{aneS}_3)_2]^{2+}$  is similar to that of  $[\text{Pd}([\text{18}] \text{aneS}_6)]^{2+}$  in  $[\text{Pd}([\text{18}] \text{aneS}_6)](\text{BPh}_4)_2$  (Figure 1b) which we have published previously.<sup>23</sup> In  $[\text{Pd}([\text{18}] \text{aneS}_6)](\text{BPh}_4)_2$  the Pd(II) ion is also located at a crystallographic inversion center coordinated to four S-donor atoms in an approximately square planar geometry with similar equatorial Pd–S distances [Pd–S4 = 2.3114(14) and Pd–S7 = 2.3067(15) Å, Table 1]. These Pd(II)–S bond lengths are similar to those of  $[\text{Pd}([\text{10}] \text{aneS}_3)_2]^{2+}$  [Pd–S = 2.330(1), 2.328(1), 3.034(1) Å].<sup>24,25</sup> The S-donors that occupy the axial positions in  $[\text{Pd}([\text{18}] \text{aneS}_6)]^{2+}$  [Pd–S1 = 3.2730(17) Å] are significantly more distant from the metal center than those in  $[\text{Pd}([\text{9}] \text{aneS}_3)_2]^{2+}$  [2.9646(8) Å] presumably reflecting the conformational constraints imposed by the  $[\text{18}] \text{aneS}_6$  ligand. Interestingly, we have also determined the single crystal structure of  $[\text{Pd}([\text{18}] \text{aneS}_6)]^{2+}$  as its  $\text{PF}_6^-$  salt (**2**). Although a similar  $[4 + 2] \text{S}_6$  co-ordination sphere is observed in  $[\text{Pd}([\text{18}] \text{aneS}_6)](\text{PF}_6)_2$  [Pd–S4 = 2.3347(18), Pd–S1 = 3.015(3) Å], the methylene chains in this structure are eclipsed contrasting with the staggered conformation observed in  $[\text{Pd}([\text{18}] \text{aneS}_6)](\text{BPh}_4)_2$  (Figure 2). The <sup>13</sup>C NMR spectrum of  $[\text{Pd}([\text{18}] \text{aneS}_6)]^{2+}$  shows a single resonance at 35.0 ppm at 293 K in  $\text{CD}_3\text{CN}$  and at 35.3 ppm at 293 K in  $d^7$ -DMF confirming equivalence of the C-centers under these conditions. Attempts to freeze out the structure in  $\text{CD}_3\text{CN}$  were unsuccessful down to 233 K, but in  $d^7$ -DMF at 209 K three resonances are observed at 39.83, 37.15, and 25.94 ppm consistent with a square planar stereochemistry for the complex in solution.

Chemical oxidation of  $[\text{Pd}([\text{9}] \text{aneS}_3)_2](\text{PF}_6)_2$  using 70%  $\text{HClO}_4$  at  $-20^\circ \text{C}$  results in the isolation of  $[\text{Pd}([\text{9}] \text{aneS}_3)_2](\text{ClO}_4)_6 \cdot (\text{H}_3\text{O})_3 \cdot (\text{H}_2\text{O})_4$  (**3**) as dark red tabular crystals. The co-ordination sphere of  $[\text{Pd}([\text{9}] \text{aneS}_3)_2]^{3+}$  in  $[\text{Pd}([\text{9}] \text{aneS}_3)_2](\text{ClO}_4)_6 \cdot (\text{H}_3\text{O})_3 \cdot (\text{H}_2\text{O})_4$  (Figure 1c) is similar to that of  $[\text{Pd}([\text{9}] \text{aneS}_3)_2]^{2+}$  (Figure 1a) except for a marked shortening of about 0.43 Å in the axial Pd–S distances to 2.5356(9) Å in  $[\text{Pd}([\text{9}] \text{aneS}_3)_2]^{3+}$  (Table 1). An elongation of the equatorial Pd–S bond lengths by about 0.05–0.06 Å accompanies the binding of the axial S-donors in  $[\text{Pd}([\text{9}] \text{aneS}_3)_2]^{3+}$  [Pd–S4 = 2.3695(8), Pd–S7 = 2.3692(8) Å] (Table 1). Thus, the co-ordination geometry of  $[\text{Pd}([\text{9}] \text{aneS}_3)_2]^{3+}$  is distorted octahedral consistent with the expected Jahn–Teller distortion for a formal  $d^7$  Pd(III) metal center.

Oxidation of  $[\text{Pd}([\text{18}] \text{aneS}_6)](\text{PF}_6)_2$  with 70%  $\text{HClO}_4$  at  $-20^\circ \text{C}$  led to the isolation of  $[\text{Pd}([\text{18}] \text{aneS}_6)](\text{ClO}_4)_6 \cdot (\text{H}_5\text{O}_2)_3$  (**4**) as dark red blocky crystals. The structure of  $[\text{Pd}([\text{18}] \text{aneS}_6)]^{3+}$  in  $[\text{Pd}([\text{18}] \text{aneS}_6)](\text{ClO}_4)_6 \cdot (\text{H}_5\text{O}_2)_3$  (Figure 1d) shows a significant shortening (ca. 0.73 Å) of the

**Table 1. Comparison of Bond Lengths (Å) and Angles (deg) for Pd(II) and Pd(III) Complexes Determined from Single Crystal X-ray Structures and Derived from DFT Calculations**

	$[\text{Pd}([\text{9}] \text{aneS}_3)_2]^{2+}$ (1)	$[\text{Pd}([\text{9}] \text{aneS}_3)_2]^{3+}$ (3)	DFT calc. $[\text{Pd}([\text{9}] \text{aneS}_3)_2]^{3+}$	$[\text{Pd}([\text{18}] \text{aneS}_6)]^{2+}$ (2)	$[\text{Pd}([\text{18}] \text{aneS}_6)]^{3+}$ (4)	DFT calc. $[\text{Pd}([\text{18}] \text{aneS}_6)]^{3+}$
Pd–S1	2.9646(8)	2.5448(15)	2.662	3.2730(17)	2.5474(6)	2.650
Pd–S4	2.3195(7)	2.3692(15)	2.416	2.3114(14)	2.3490(6)	2.421
Pd–S7	2.3085(7)	2.3558(14)	2.414	2.3067(15)	2.3454(5)	2.419
S1–Pd–S4	94.42(3)	87.33(5)	85.14	75.06(5)	89.08(2)	86.52
S1–Pd–S7	95.69(3)	87.17(5)	87.68	103.88(5)	89.48(2)	86.46
S4–Pd–S7	89.13(3)	88.88(5)	85.85	86.24(5)	88.191(19)	91.21

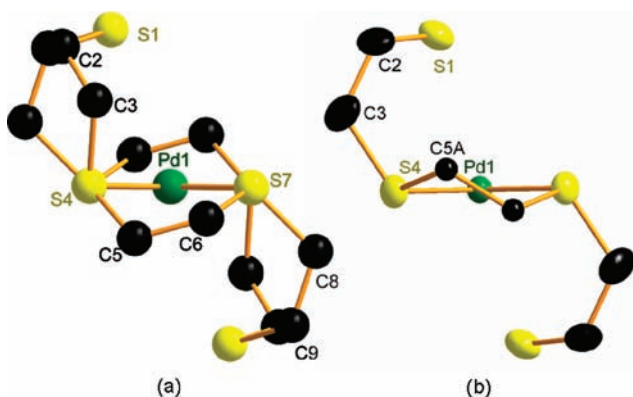


**Figure 2.** View of the crystal structures of  $[\text{Pd}([\text{18}]\text{aneS}_6)]^{2+}$ .

axial Pd–S distances to 2.5474(6) Å (Table 1), an increase in the angle which the Pd–S1 vector makes with the S4–Pd–S7 plane from 68.64(5)° (BPh<sub>4</sub><sup>−</sup> salt) or 75.37(7)° (PF<sub>6</sub><sup>−</sup> salt) of  $[\text{Pd}([\text{18}]\text{aneS}_6)]^{2+}$  to 87.97(2)° in  $[\text{Pd}([\text{18}]\text{aneS}_6)]^{3+}$ , and a slight elongation in the equatorial Pd–S bond lengths [Pd–S4 = 2.3490(6), Pd–S7 = 2.3454(5) Å in  $[\text{Pd}([\text{18}]\text{aneS}_6)]^{3+}$  versus Pd–S4 = 2.3114(14), Pd–S7 = 2.3067(15) Å in  $[\text{Pd}([\text{18}]\text{aneS}_6)](\text{BPh}_4)_2$  (Table 1). Thus, oxidation of  $[\text{Pd}([\text{18}]\text{aneS}_6)]^{2+}$  to  $[\text{Pd}([\text{18}]\text{aneS}_6)]^{3+}$  results in a larger structural change that is associated with the oxidation of  $[\text{Pd}([\text{9}]\text{aneS}_3)_2]^{2+}$  to  $[\text{Pd}([\text{9}]\text{aneS}_3)_2]^{3+}$ , but affords in both cases distorted octahedral geometries at Pd<sup>III</sup> satisfying the requirements of formal d<sup>7</sup> metal centers that are subject to a Jahn–Teller distortions.

**Electrochemistry of  $[\text{Pd}([\text{9}]\text{aneS}_3)_2](\text{PF}_6)_2$ .** The cyclic voltammogram of  $[\text{Pd}([\text{9}]\text{aneS}_3)_2](\text{PF}_6)_2$  in MeCN (0.2 M NBu<sub>4</sub>PF<sub>6</sub>, 243 K) (Figure 3a) shows a reversible oxidation process at  $E_{1/2} = +0.57$  V vs. Fc<sup>+</sup>/Fc (Figure 3b), a reductive process at  $E_p^a = -0.69$  V (Figure 3c), and a quasi-reversible oxidation process centered at  $E_{1/2} = +0.97$  V vs. Fc<sup>+</sup>/Fc (Figure 3d). Coulometric measurements confirm the oxidation process at  $E_{1/2} = +0.57$  V and the reduction process at  $E_{1/2} = -0.69$  V as one-electron processes and are assigned to Pd(III)/Pd(II) and Pd(II)/Pd(I) couples, respectively. Related oxidative redox processes have been observed for  $[\text{Pd}([\text{10}]\text{aneS}_3)_2]^{3/2+}$  at  $E_{1/2} = +0.61$  V<sup>26</sup> and  $[\text{Pd}([\text{18}]\text{aneS}_4\text{N}_2)]^{3/2+}$  at  $E_{1/2} = +0.57$  V.<sup>27a</sup>

The  $[\text{Pd}([\text{9}]\text{aneS}_3)_2]^{2+/3+}$  couple was probed by in situ UV/vis spectroelectrochemistry in MeCN (0.2 M NBu<sub>4</sub>PF<sub>6</sub>, 243 K) at +0.70 V vs. Fc<sup>+</sup>/Fc under N<sub>2</sub> (Figure 4). The oxidation of  $[\text{Pd}([\text{9}]\text{aneS}_3)_2]^{2+}$  [ $\lambda_{\text{max}} = 619$  nm ( $\epsilon_{\text{max}} = 56$  L mol<sup>−1</sup> cm<sup>−1</sup>) 294 (15000)] is accompanied by the growth of three new absorptions at  $\lambda_{\text{max}} = 470$  nm ( $\epsilon_{\text{max}} = 9650$  L mol<sup>−1</sup> cm<sup>−1</sup>), 339 nm (26400), and 235 nm (14900), with isosbestic points at  $\lambda_{\text{iso}} = 214, 259, 390,$  and 588 nm. Subsequent reduction at +0.30 V vs. Fc<sup>+</sup>/Fc regenerates the original UV/vis spectrum of  $[\text{Pd}([\text{9}]\text{aneS}_3)_2]^{2+}$ . Thus, the  $[\text{Pd}([\text{9}]\text{aneS}_3)_2]^{2+/3+}$  couple is fully chemical reversible at 243 K. The relative intensities of the absorptions at 339 and 235 nm for  $[\text{Pd}([\text{9}]\text{aneS}_3)_2]^{3+}$  suggests that these transitions possess charge-transfer character involving the thioether S donors.

A deep-red solution of  $[\text{Pd}([\text{9}]\text{aneS}_3)_2]^{3+}$  was prepared by the controlled potential electrolysis of  $[\text{Pd}([\text{9}]\text{aneS}_3)_2]^{2+}$  in MeCN containing NBu<sub>4</sub>PF<sub>6</sub> (0.2 M) at +0.7 V vs. Fc<sup>+</sup>/Fc at 273 K. The X-band EPR spectrum of this electrochemically

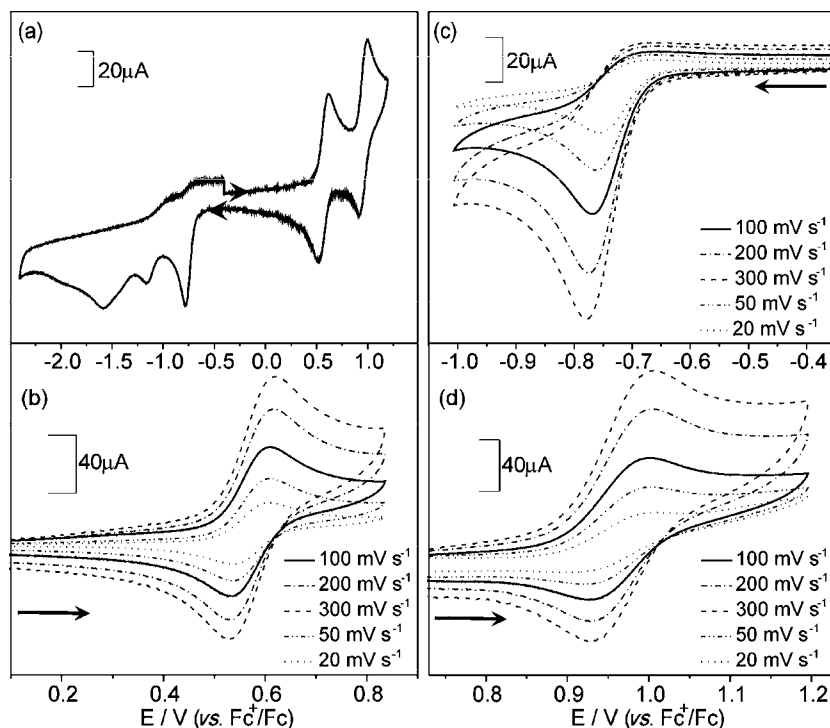


**Figure 3.** (a) Cyclic voltammogram of  $[\text{Pd}([\text{9}]\text{aneS}_3)_2](\text{PF}_6)_2$ . (b) Cyclic voltammogram of the oxidation process of  $[\text{Pd}([\text{9}]\text{aneS}_3)_2](\text{PF}_6)_2$  at +0.57 V assigned to a formal Pd(III)/Pd(II) couple. (c) Reduction process for  $[\text{Pd}([\text{9}]\text{aneS}_3)_2](\text{PF}_6)_2$  at −0.73 V assigned to a formal Pd(II)/Pd(I) couple. (d) Cyclic voltammogram of the oxidation process of  $[\text{Pd}([\text{9}]\text{aneS}_3)_2](\text{PF}_6)_2$  at +0.97 V. All measurements were made in MeCN with NBu<sub>4</sub>PF<sub>6</sub> (0.2 M) as a supporting electrolyte at 273 K and are shown at a scan rate of 100 mV s<sup>−1</sup> with the varied scan rates of 300, 200, 50, and 20 mV s<sup>−1</sup> shown as dotted traces.

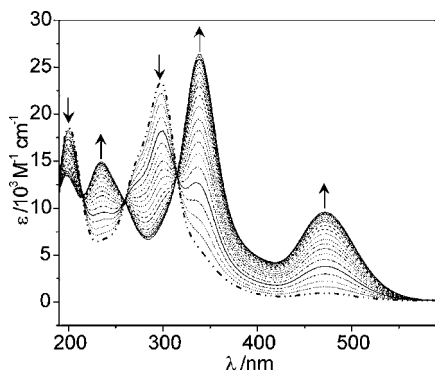


**Figure 4.** In situ UV/vis spectra of the oxidation of  $[\text{Pd}([9]\text{aneS}_3)_2](\text{PF}_6)_2$  in MeCN (0.2 M  $\text{NBu}_4\text{PF}_6$ ) at 273 K at +0.7 V vs.  $\text{Fc}^+/\text{Fc}$ .  $[\text{Pd}([9]\text{aneS}_3)_2]^{2+}$  is shown as a dotted trace.

generated species was recorded as fluid (ambient) and frozen (77 K) solutions and was found to be the same as that of the chemically generated species recorded in  $\text{HClO}_4$ . The electrochemically generated sample decomposed slowly in MeCN (0.2 M  $\text{NBu}_4\text{PF}_6$ ) to give the pale green-blue, EPR-silent  $[\text{Pd}([9]\text{aneS}_3)_2]^{2+}$ .

The reduction process for  $[\text{Pd}([9]\text{aneS}_3)_2](\text{PF}_6)_2$  was also investigated using EPR spectroscopy. A brown-red solution of  $[\text{Pd}([9]\text{aneS}_3)_2]^+$  was prepared by the controlled potential electrolysis of  $[\text{Pd}([9]\text{aneS}_3)_2]^{2+}$  in MeCN containing  $\text{NBu}_4\text{PF}_6$  (0.2 M) at  $-0.85$  V vs.  $\text{Fc}^+/\text{Fc}$  at 273 K. The X-band EPR spectrum of this electrochemically generated species was recorded as fluid and frozen solutions (77 K). Both spectra are poorly defined (Supporting Information, Figure S11),

although the profile of the frozen solution spectrum appears to be approximately axial with some evidence of Pd satellites associated with coupling to the  $^{105}\text{Pd}$  ( $I = 5/2$ , 22.3%) nucleus.<sup>27b</sup>

Cyclic voltammetry of  $[\text{Pd}([18]\text{aneS}_6)](\text{PF}_6)_2$  in MeCN containing  $\text{NBu}_4\text{PF}_6$  over the potential range of +2 to  $-2$  V vs  $\text{Fc}^+/\text{Fc}$  at 273 K did not reveal any significant current responses associated with well-defined reduction or oxidation processes for  $[\text{Pd}([18]\text{aneS}_6)]^{3+}$ . Thus, under these conditions, electrochemical oxidation of this complex is inhibited kinetically, most likely because of the potentially axially bound S-donors being displaced away from the metal center to give a square planar Pd(II) complex in solution. Given the lower resolution of the X-band EPR spectra recorded for electrochemically generated  $[\text{Pd}([9]\text{aneS}_3)_2]^{3+}$  and the poorly defined electrochemistry of  $[\text{Pd}([18]\text{aneS}_6)]^{3+}$ , we carried out multifrequency EPR spectroscopic studies on chemically generated  $[\text{Pd}([9]\text{aneS}_3)_2]^{3+}$  and  $[\text{Pd}([18]\text{aneS}_6)]^{3+}$ .

**Multifrequency EPR Spectroscopic Studies on  $[\text{Pd}([9]\text{aneS}_3)_2]^{3+}$  and  $[\text{Pd}([18]\text{aneS}_6)]^{3+}$ .** The Pd(III) complex  $[\text{Pd}([9]\text{aneS}_3)_2]^{3+}$  was studied by EPR spectroscopy as fluid (233 K) and as frozen (77 K) solutions at X-band frequency (Figures 5 and 6). The fluid X-band EPR spectrum recorded in 70%  $\text{HClO}_4$  is dominated by the central Pd ( $I = 0$ , 77.7%) feature and shows two lines of the expected six-line hyperfine pattern resulting from coupling to the  $^{105}\text{Pd}$  ( $I = 5/2$ , 22.3%) nucleus. Simulation of the X-band fluid spectrum gave  $g_{\text{iso}} = 2.024$ ,  $|A_{\text{iso}(\text{Pd})}| = 18.9 \times 10^{-4} \text{ cm}^{-1}$  (56.7 MHz),  $W_{\text{iso}} = 57$  MHz for  $[\text{Pd}([9]\text{aneS}_3)_2]^{3+}$ . The frozen solution X-band EPR spectra of  $[\text{Pd}([9]\text{aneS}_3)_2]^{3+}$ , prepared electrochemically (MeCN, 0.2 M  $\text{NBu}_4\text{PF}_6$ ) or chemically with  $\text{HClO}_4$  (Figure 5b), possess

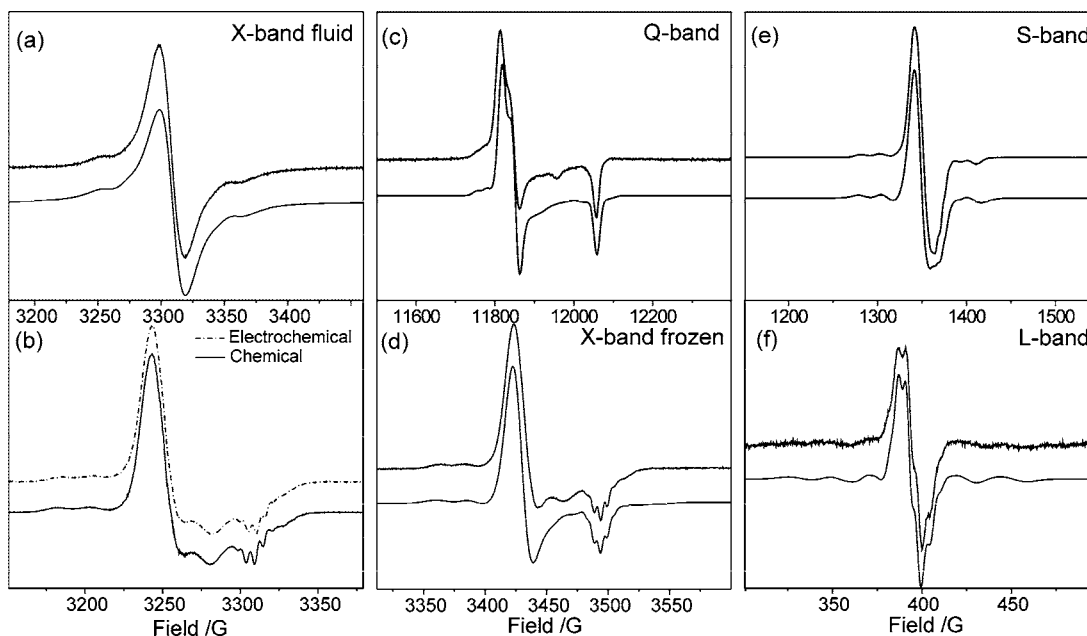


**Figure 5.** (a) X-band fluid spectrum of  $[\text{Pd}([9]\text{aneS}_3)_2]^{3+}$  in 70%  $\text{HClO}_4$  at 233 K. Simulation gives  $g_{\text{iso}} = 2.024$ ,  $|A_{\text{iso}(\text{Pd})}| = 18.9 \times 10^{-4} \text{ cm}^{-1}$  (56.7 MHz),  $W_{\text{iso}} = 57$  MHz. (b) Comparison of the X-band EPR frozen solution spectrum of electrochemically (in MeCN, 0.2 M  $\text{NBu}_4\text{PF}_6$ ) and chemically generated (in  $\text{HClO}_4$ )  $[\text{Pd}([9]\text{aneS}_3)_2]^{3+}$  at 77 K. Multifrequency EPR frozen spectra of  $[\text{Pd}([9]\text{aneS}_3)_2]^{3+}$  in 70%  $\text{HClO}_4$  at 50 K at (c) Q-band, (d) X-band, (e) S-band, and (f) L-band. Simulation gave  $g_{\text{xx}} = 2.046$ ,  $g_{\text{yy}} = 2.041$ ,  $g_{\text{zz}} = 2.004$ ;  $|A_{\text{xx}(\text{Pd})}| = 24 \times 10^{-4} \text{ cm}^{-1}$  (72 MHz),  $|A_{\text{yy}(\text{Pd})}| = 22 \times 10^{-4} \text{ cm}^{-1}$  (66 MHz),  $|A_{\text{zz}(\text{Pd})}| = 14 \times 10^{-4} \text{ cm}^{-1}$  (42 MHz);  $|a_{\text{xx}}(^1\text{H})| = 4 \times 10^{-4} \text{ cm}^{-1}$  (12 MHz),  $|a_{\text{yy}}(^1\text{H})| = 5 \times 10^{-4} \text{ cm}^{-1}$  (15 MHz),  $|a_{\text{zz}}(^1\text{H})| = 5.5 \times 10^{-4} \text{ cm}^{-1}$  (16.5 MHz),  $|A_{\text{zz}(\text{Pd})}| = 14 \times 10^{-4} \text{ cm}^{-1}$ ;  $|a_{\text{xx}}(^1\text{H})| = 4 \times 10^{-4} \text{ cm}^{-1}$ ,  $|a_{\text{yy}}(^1\text{H})| = 5 \times 10^{-4} \text{ cm}^{-1}$ ,  $|a_{\text{zz}}(^1\text{H})| = 5.5 \times 10^{-4} \text{ cm}^{-1}$ ,  $A\text{-strain}$  ( $^{105}\text{Pd}$ ):  $AS_{\text{xx}} = 15$  MHz,  $AS_{\text{yy}} = 25$  MHz,  $AS_{\text{zz}} = 30$  MHz with linewidths of (c)  $W_{\text{xx}} = 60$  MHz,  $W_{\text{yy}} = 34$  MHz,  $W_{\text{zz}} = 12.5$  MHz; (d)  $W_{\text{xx}} = 60$  MHz,  $W_{\text{yy}} = 57$  MHz,  $W_{\text{zz}} = 50$  MHz; (e)  $W_{\text{xx}} = 37$  MHz,  $W_{\text{yy}} = 25$  MHz,  $W_{\text{zz}} = 18$  MHz; and (f)  $W_{\text{xx}} = 15$  MHz,  $W_{\text{yy}} = 13$  MHz,  $W_{\text{zz}} = 12.5$  MHz. Upper traces: experimental spectra; lower traces: simulations.

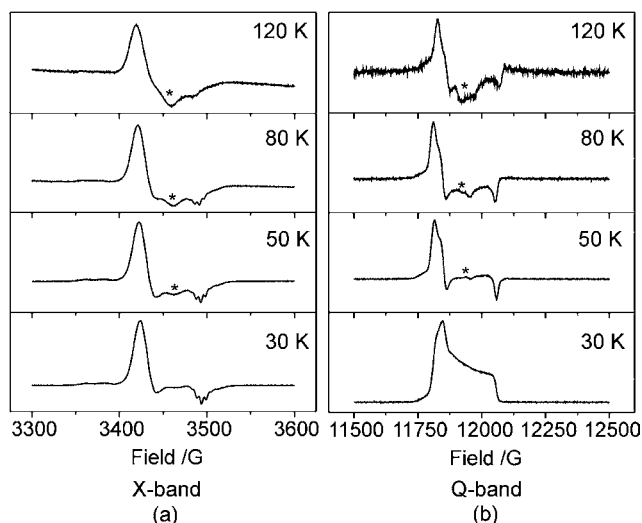


**Figure 6.** X-band and Q-band EPR spectra of  $[\text{Pd}([\text{9}]\text{aneS}_3)_2]^{3+}$  in  $\text{HClO}_4$  at 30, 50, 80, and 120 K. Features in the spectra attributed to a dynamic Jahn–Teller process are indicated with \*.

approximately axial profiles with  $g_{xx} \sim g_{yy} > g_{zz}$ .  $^{105}\text{Pd}$  coupling extends across each spectrum, and coupling involving a second nuclear spin is resolved in the  $g_{zz}$  region. Satisfactory simulations of the frozen solution X-band spectra could not be obtained because of a clear distortion in the central region of each spectrum recorded at 77 K assigned to dynamic effects (Figure 6). Our recent studies on the analogous  $d^7$  metal center  $[\text{Ni}([\text{9}]\text{aneS}_3)_2]^{3+}$  revealed temperature dependent dynamic Jahn–Teller distortions which influence significantly the profile of the EPR spectra recorded over a range of temperatures. In our studies of  $[\text{Ni}([\text{9}]\text{aneS}_3)_2]^{3+}$ ,<sup>28</sup> we addressed these effects by recording EPR spectra between 5–200 K to obtain data that could be simulated satisfactorily. We have employed this approach in this study to record suitable data for  $[\text{Pd}([\text{9}]\text{aneS}_3)_2]^{3+}$ . Thus, a multifrequency variable-temperature study from 5–120 K was conducted at Q-, X-, S-, and L-band frequencies on chemically generated solutions of  $[\text{Pd}([\text{9}]\text{aneS}_3)_2]^{3+}$  in 70%  $\text{HClO}_4$ .

Between 5 and 30 K saturation led to absorption-like profiles in the spectra of  $[\text{Pd}([\text{9}]\text{aneS}_3)_2]^{3+}$  in 70%  $\text{HClO}_4$  at X- and Q-band frequencies (Figure 6). Between 80 and 120 K the  $g$ -values shift and the anisotropy in each spectrum is lost, with an almost isotropic signal recorded at 120 K. The spectra at 50 K were chosen for study, since suitable spectra could be obtained at S-, L-, X-, and Q-band frequencies and were the lowest temperature data that could be obtained that did not exhibit saturation effects. The  $g_{zz}$  Pd ( $I = 0$ ) feature in the X- and L-band spectra possesses a resolved five-line superhyperfine pattern. We have observed similar couplings previously in  $[\text{Pt}([\text{9}]\text{aneS}_3)_2]^{3+}$ ,<sup>20</sup> and these have been assigned to hyperfine coupling involving four equivalent hydrogen nuclei derived from the backbone of the [9]aneS<sub>3</sub> ligand. We confirmed this assignment by generating  $[\text{Pd}([\text{9}]\text{aneS}_3)_2]^{3+}$  in  $\text{DClO}_4$  to rule out the possibility of proton coupling involving the solvent. Satisfactory simultaneous simulation of the S-, L-, X-, and Q-band spectra gave  $g_{xx} = 2.046$ ,  $g_{yy} = 2.041$ ,  $g_{zz} = 2.004$ ;  $|A_{xx(\text{Pd})}| = 24 \times 10^{-4} \text{ cm}^{-1}$  (72 MHz),  $|A_{yy(\text{Pd})}| = 22 \times 10^{-4} \text{ cm}^{-1}$  (66 MHz),  $|A_{zz(\text{Pd})}| = 14 \times 10^{-4} \text{ cm}^{-1}$  (42 MHz);  $|a_{xx}(\text{H})| = 4 \times 10^{-4} \text{ cm}^{-1}$  (12 MHz),  $|a_{yy}(\text{H})| = 5 \times 10^{-4} \text{ cm}^{-1}$  (15 MHz),  $|a_{zz}(\text{H})| = 5.5 \times 10^{-4} \text{ cm}^{-1}$  (16.5 MHz) (Figure 5). The superhyperfine coupling  $[a_{ii}(\text{H})]$   $a_{ii}$  ( $ii = xx = yy = zz$ ) was

simulated by the inclusion of coupling to four equivalent  $^1\text{H}$  nuclei.  $A$ -strain ( $AS_{ii}$ )<sup>29</sup> in the  $^{105}\text{Pd}$  component, in addition to the usual inhomogeneous line-broadening, ( $W_{ij}$ ,  $i = x, y, z$ ) was included in the simulations to give  $A$ -strain ( $^{105}\text{Pd}$ ):  $AS_{xx} = 15 \text{ MHz}$ ,  $AS_{yy} = 25 \text{ MHz}$ ,  $AS_{zz} = 30 \text{ MHz}$ .

The Pd(III) complex  $[\text{Pd}([\text{18}]\text{aneS}_6)]^{3+}$  generated in 70%  $\text{HClO}_4$  was also studied using EPR spectroscopy. A fluid solution at 233 K was recorded at X-band (Figure 7a) and

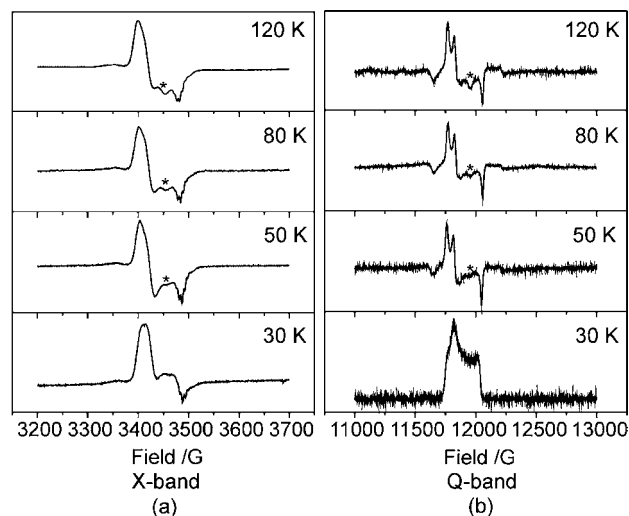


**Figure 7.** X-band and Q-band EPR spectra of  $[\text{Pd}([\text{18}]\text{aneS}_6)]^{3+}$  in 70%  $\text{HClO}_4$  at 30, 50, 80, and 120 K. Features in the spectra attributed to a dynamic Jahn–Teller process are indicated with \*.

could be simulated with  $g_{iso} = 2.015$ ,  $W_{iso} = 155 \text{ MHz}$  with an estimate of  $|A_{iso(\text{Pd})}| = 18.8 \times 10^{-4} \text{ cm}^{-1}$  (56.4 MHz).  $^{105}\text{Pd}$  satellites are not visibly resolved, but contribute to the broad linewidth (Figure 8a). The EPR spectra of  $[\text{Pd}([\text{18}]\text{aneS}_6)]^{3+}$  exhibited similar dynamic Jahn–Teller  $g$ -value averaging to that observed for  $[\text{Pd}([\text{9}]\text{aneS}_3)_2]^{3+}$  and which was temperature dependent. However, this dependency was not as visibly pronounced as that observed for  $[\text{Pd}([\text{9}]\text{aneS}_3)_2]^{3+}$ . Nevertheless we undertook a multifrequency, variable temperature EPR spectroscopic study to determine the temperature at which the distortions in the spectra, associated with a dynamic Jahn–Teller distortion, are minimized across all frequencies. We found that the data recorded at 50 K could be simulated satisfactorily.

The multifrequency EPR frozen spectra of  $[\text{Pd}([\text{18}]\text{aneS}_6)]^{3+}$  in 70%  $\text{HClO}_4$  at 50 K possess rhombic features and exhibit resolved  $^{105}\text{Pd}$  couplings which extend across the spectrum at each frequency. The X- and S-band data also show a five-line superhyperfine splitting pattern associated with the Pd  $I = 0$  feature in the  $g_{zz}$  region of the spectrum. This feature is similar to that observed in the X- and L-band spectra of  $[\text{Pd}([\text{9}]\text{aneS}_3)_2]^{3+}$  (see above) and  $[\text{Pt}([\text{9}]\text{aneS}_3)_2]^{3+}$  reported previously.<sup>20</sup> The X-, Q- and S-band spectra could be simulated simultaneously with the parameters  $g_{xx} = 2.048$ ,  $g_{yy} = 2.036$ ,  $g_{zz} = 1.998$ ;  $|A_{xx(\text{Pd})}| = 23 \times 10^{-4} \text{ cm}^{-1}$  (69 MHz),  $|A_{yy(\text{Pd})}| = 22 \times 10^{-4} \text{ cm}^{-1}$  (66 MHz),  $|A_{zz(\text{Pd})}| = 4 \times 10^{-4} \text{ cm}^{-1}$  (12 MHz);  $|a_{xx}(\text{H})| = |a_{yy}(\text{H})| = 5 \times 10^{-4} \text{ cm}^{-1}$  (15 MHz),  $|a_{zz}(\text{H})| = 6 \times 10^{-4} \text{ cm}^{-1}$  (18 MHz) (Figure 8). Satisfactory simulation of the superhyperfine features required the inclusion of  $A$ -strain in the simulations:  $A$ -strain ( $^{105}\text{Pd}$ )  $AS_{xx} = 20 \text{ MHz}$ ,  $AS_{yy} = 20 \text{ MHz}$ ,  $AS_{zz} = 20 \text{ MHz}$ .

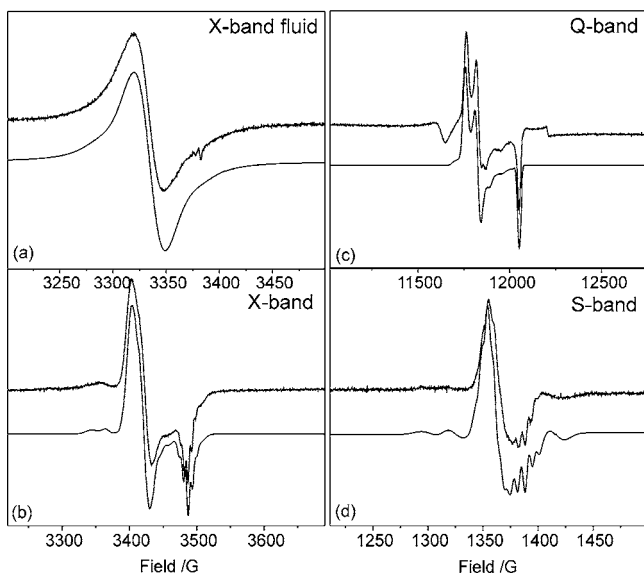


**Figure 8.** (a) X-band fluid spectrum of  $[\text{Pd}([\text{18}]\text{aneS}_3)_2]^{3+}$  in 70%  $\text{HClO}_4$  at 233 K. Simulation gives  $g_{\text{iso}} = 2.015$ ,  $|A_{\text{iso}(\text{Pd})}| = 18.8 \times 10^{-4} \text{ cm}^{-1}$  (56.4 MHz),  $W_{\text{iso}} = 155 \text{ MHz}$ . Multifrequency EPR frozen spectra of  $[\text{Pd}([\text{18}]\text{aneS}_6)]^{3+}$  in 70%  $\text{HClO}_4$  at 50 K at (b) X-band, (c) Q-band and (d) S-band. Simulation using all of the multifrequency data gives  $g_{\text{xx}} = 2.048$ ,  $g_{\text{yy}} = 2.036$ ,  $g_{\text{zz}} = 1.998$ ;  $|A_{\text{xx}(\text{Pd})}| = 23 \times 10^{-4} \text{ cm}^{-1}$  (69 MHz),  $|A_{\text{yy}(\text{Pd})}| = 22 \times 10^{-4} \text{ cm}^{-1}$  (66 MHz),  $|A_{\text{zz}(\text{Pd})}| = 4 \times 10^{-4} \text{ cm}^{-1}$  (12 MHz);  $|a_{\text{xx}}(\text{H})| = |a_{\text{yy}}(\text{H})| = 5 \times 10^{-4} \text{ cm}^{-1}$  (15 MHz),  $|a_{\text{zz}}(\text{H})| = 6 \times 10^{-4} \text{ cm}^{-1}$  (18 MHz) with linewidths of (b)  $W_{\text{xx}} = 20 \text{ MHz}$ ,  $W_{\text{yy}} = 19 \text{ MHz}$ ,  $W_{\text{zz}} = 14 \text{ MHz}$ ; (c)  $W_{\text{xx}} = 70 \text{ MHz}$ ,  $W_{\text{yy}} = 75 \text{ MHz}$ ,  $W_{\text{zz}} = 30 \text{ MHz}$ ; (d)  $W_{\text{xx}} = 15 \text{ MHz}$ ,  $W_{\text{yy}} = 17 \text{ MHz}$ ,  $W_{\text{zz}} = 13 \text{ MHz}$ . A-strain ( $^{105}\text{Pd}$ ):  $AS_{\text{xx}} = 20 \text{ MHz}$ ,  $AS_{\text{yy}} = 20 \text{ MHz}$ ,  $AS_{\text{zz}} = 20 \text{ MHz}$ . Upper traces: experimental spectra; lower traces: simulations.

**Interpretation of the EPR Data of  $[\text{Pd}([\text{9}]\text{aneS}_3)_2]^{3+}$  and  $[\text{Pd}([\text{18}]\text{aneS}_6)]^{3+}$ .** We followed the approach described in our studies of  $[\text{Au}([\text{9}]\text{aneS}_3)_2]^{2+21}$  and  $[\text{Au}([\text{9}]\text{aneS}_2\text{O})_2]^{2+30}$  to interpret the EPR spectra of  $[\text{Pd}([\text{9}]\text{aneS}_3)_2]^{3+}$  and  $[\text{Pd}([\text{18}]\text{aneS}_6)]^{3+}$ . Thus,  $g_{\text{xx}}$  and  $g_{\text{yy}}$  are assigned to orientations lying in the equatorial plane, with  $g_{\text{zz}}$  (the lowest  $g$ -value) perpendicular to this plane. Crystal field theory arguments place the unpaired electron in the Pd  $4d_{z^2}$  orbital for  $[\text{Pd}([\text{9}]\text{aneS}_3)_2]^{3+}$  and  $[\text{Pd}([\text{18}]\text{aneS}_6)]^{3+}$ . Density functional theory (DFT) calculations are consistent with this interpretation, (see below), and predict a singly occupied molecular orbital (SOMO) of  $a_g$  symmetry in  $C_i$  symmetry for  $[\text{Pd}([\text{9}]\text{aneS}_3)_2]^{3+}$  and  $[\text{Pd}([\text{18}]\text{aneS}_6)]^{3+}$  and that the dominant metal contribution of the SOMO is from the Pd  $4d_{z^2}$  orbital. The nature of the SOMO is consistent with the observed  $g_{\text{xx}} \sim g_{\text{yy}} > g_{\text{zz}} > g_e$  pattern in the EPR spectra of these complexes. In these cases the spin Hamiltonian parameters can be treated by perturbation theory:<sup>31</sup>

$$\Delta g_{\text{xx}} = \frac{6\lambda}{\delta_{xy}} = g_{\text{xx}} - g_e \quad (1)$$

$$\Delta g_{\text{yy}} = \frac{6\lambda}{\delta_{xz}} = g_{\text{yy}} - g_e \quad (2)$$

$$\Delta g_{\text{zz}} = 0 \quad (3)$$

$$\frac{A_{\text{xx}(\text{Pd})} - A_s}{P_d} = -\frac{2}{7}a^2 + \Delta g_{\text{xx}} + \frac{1}{14}\Delta g_{\text{yy}} \quad (4)$$

$$\frac{A_{\text{yy}(\text{Pd})} - A_s}{P_d} = -\frac{2}{7}a^2 + \Delta g_{\text{yy}} + \frac{1}{14}\Delta g_{\text{xx}} \quad (5)$$

$$\frac{A_{\text{zz}(\text{Pd})} - A_s}{P_d} = \frac{4}{7}a^2 - \frac{1}{14}(\Delta g_{\text{xx}} + \Delta g_{\text{yy}}) \quad (6)$$

where  $g_e$  is the  $g$ -value of the free electron 2.0023,  $\lambda$  is the spin-orbit coupling constant for Pd with a  $4d^7$  electronic configuration,  $\delta$  is the weighted average energy gap between ground state and excited states,  $P_d$  ( $-71.8 \times 10^{-4} \text{ cm}^{-1}$ ) is the electron-nuclear dipolar coupling parameter for a  $4d^7$  Pd center derived using the methodology described by Rieger,<sup>32</sup>  $a^2$  is the linear combination of atomic orbitals (LCAO) coefficient of the Pd  $4d_{z^2}$  orbital in the SOMO, and  $A_s$  is the isotropic Fermi contact term.

$$A_s = \left( \frac{A_{\text{xx}} + A_{\text{yy}} + A_{\text{zz}}}{3} \right) - P_d \left( \frac{\Delta g_{\text{xx}} + \Delta g_{\text{yy}}}{3} \right)$$

Equations 1–6 can be combined to give eq 7:

$$A_{\text{zz}(\text{Pd})} = \left( \frac{A_{\text{xx}} + A_{\text{yy}} + A_{\text{zz}}}{3} \right) + P_d \left[ \frac{4}{7}a^2 - \frac{17}{42}(\Delta g_{\text{xx}} + \Delta g_{\text{yy}}) \right] \quad (7)$$

From eqs 1–6 we expect  $g_{\text{xx}}$  and  $g_{\text{yy}} > g_{\text{zz}}$  with  $g_{\text{zz}}$  being the smallest  $g$ -value, oriented approximately along the axis of the formal  $d_{z^2}$  orbital, and this is the basis of our assignment of the orientation of the  $z$ -axis. Equations 1–6 assume that the principal axes of the  $g$ - and  $A$ -matrices are coincident, and we have assumed this to be the case experimentally because we achieve good simulations without including noncoincidence effects. However, it should be noted that noncoincidence could occur for the  $C_i$  molecular point symmetries of  $[\text{Pd}([\text{9}]\text{aneS}_3)_2]^{3+}$  and  $[\text{Pd}([\text{18}]\text{aneS}_6)]^{3+}$  because in this symmetry all of the 4d orbitals transform as  $a_g$  and can therefore mix. Any such scrambling of d-orbital functions can give rise to  $g$ - and  $A$ -matrix noncoincidence effects.<sup>31</sup> DFT calculations (see later) suggest that the dominant 4d metal contribution to the SOMO is  $4d_{z^2}$  and that there are no contributions from the other 4d orbitals of  $a_g$  symmetry. Thus, any noncoincidence effects in  $[\text{Pd}([\text{9}]\text{aneS}_3)_2]^{3+}$  and  $[\text{Pd}([\text{18}]\text{aneS}_6)]^{3+}$  are likely to be minor.

The solution of eq 7 with  $g$  and  $|A_{(\text{Pd})}|$  values derived from the EPR simulations gives for  $[\text{Pd}([\text{9}]\text{aneS}_3)_2]^{3+}$ :  $a^2 = 20.4\%$  with  $A_{\text{iso}} = 18.9 \times 10^{-4} \text{ cm}^{-1}$ ,  $A_{\text{xx}(\text{Pd})} = A_{\text{yy}(\text{Pd})} = 23 \times 10^{-4} \text{ cm}^{-1}$ , and  $A_{\text{zz}(\text{Pd})} = 4 \times 10^{-4} \text{ cm}^{-1}$ . For  $[\text{Pd}([\text{18}]\text{aneS}_6)]^{3+}$   $A_{\text{iso}}$  is unresolved in the fluid EPR spectra and following the assignments of the signs of the principal  $A_{ii(\text{Pd})}$  ( $i = x, y$  or  $z$ ) values for  $[\text{Pd}([\text{9}]\text{aneS}_3)_2]^{3+}$ , together with the total metal character in the SOMO revealed by DFT calculations on a model of  $[\text{Pd}([\text{18}]\text{aneS}_6)]^{3+}$ , give:  $a^2 = 25.0\%$  with  $A_{\text{xx}(\text{Pd})} = 23 \times 10^{-4} \text{ cm}^{-1}$ ,  $A_{\text{yy}(\text{Pd})} = 22 \times 10^{-4} \text{ cm}^{-1}$ , and  $A_{\text{zz}(\text{Pd})} = 4 \times 10^{-4} \text{ cm}^{-1}$ ;  $a^2 = 18.0\%$  with  $A_{\text{xx}(\text{Pd})} = 23 \times 10^{-4} \text{ cm}^{-1}$ ,  $A_{\text{yy}(\text{Pd})} = 22 \times 10^{-4} \text{ cm}^{-1}$ , and  $A_{\text{zz}(\text{Pd})} = -4 \times 10^{-4} \text{ cm}^{-1}$ . Comparison with the composition of the SOMOs from DFT calculations of  $[\text{Pd}([\text{9}]\text{aneS}_3)_2]^{3+}$  and  $[\text{Pd}([\text{18}]\text{aneS}_6)]^{3+}$  (see below) suggest that of these two potential options  $a^2 = 25.0\%$  is more appropriate.

**DFT Calculations of  $[\text{Pd}([\text{9}] \text{aneS}_3)_2]^{3+}$  and  $[\text{Pd}([\text{18}] \text{aneS}_6)]^{3+}$ .** The experimental and calculated structural parameters for the  $\text{PdS}_6$  co-ordination spheres of models of  $[\text{Pd}([\text{9}] \text{aneS}_3)_2]^{3+}$  and  $[\text{Pd}([\text{18}] \text{aneS}_6)]^{3+}$  are compared in Table 1, and the coordinate frames employed in the calculations are shown in Figures 9a and 9b, respectively. The

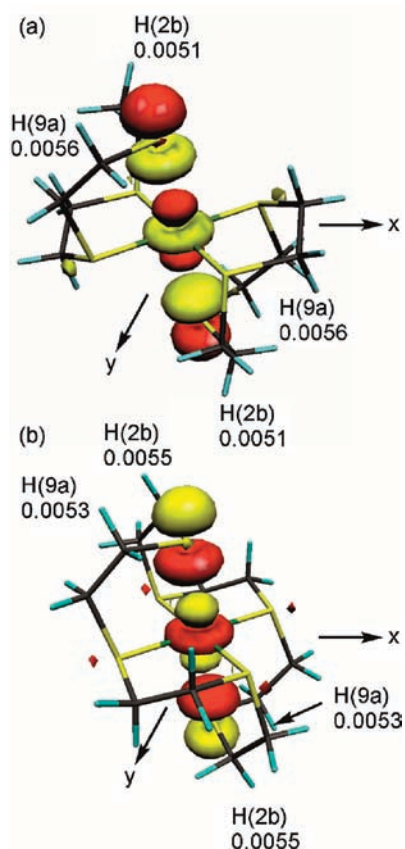


**Figure 9.** Isosurface plots of the  $\alpha$ -spin SOMO of (a)  $[\text{Pd}([\text{9}] \text{aneS}_3)_2]^{3+}$  and (b)  $[\text{Pd}([\text{18}] \text{aneS}_6)]^{3+}$  derived from BP-TZP relativistic DFT calculations with spin density values for the protons H2b, H9a and their symmetry equivalents.

ZORA SR DFT calculations employed all-electron TZP basis sets derived from the ZORA/TZP database of the ADF suite of programs. We have shown that this level of calculation reproduces the principal features of the geometric and

electronic structures of  $[\text{Au}([\text{9}] \text{aneS}_3)_2]^{2+}$ ,<sup>21</sup>  $[\text{Au}([\text{9}] \text{aneS}_2\text{O})_2]^{2+}$ ,<sup>30</sup>  $[\text{Ag}([\text{18}] \text{aneS}_4\text{O}_2)]^{2+}$ ,<sup>33</sup>  $[\text{Ni}([\text{9}] \text{aneNS}_2-\text{CH}_3)_2]^{3+}$ ,  $[\text{Ni}(\text{bis}[\text{9}] \text{aneNS}_2-\text{C}_2\text{H}_4)]^{3+}$ ,  $[\text{Ni}([\text{9}] \text{aneS}_3)_2]^{3+}$ ,<sup>28</sup> and  $[\text{Pt}([\text{9}] \text{aneS}_3)_2]^{3+}$ .<sup>20</sup> For  $[\text{Pd}([\text{9}] \text{aneS}_3)_2]^{3+}$ , the geometry optimized structures reveal axial and equatorial Pd–S distances that are about 0.12 and 0.05 Å longer, respectively, and S–Pd–S bond angles that differ by about 1.8° from those for the experimentally determined structure of  $[\text{Pd}([\text{9}] \text{aneS}_3)_2]^{3+}$  in  $[\text{Pd}([\text{9}] \text{aneS}_3)_2](\text{ClO}_4)_6 \cdot (\text{H}_3\text{O})_3 \cdot (\text{H}_2\text{O})_4$ . In the calculated structure of  $[\text{Pd}([\text{18}] \text{aneS}_6)]^{3+}$  the equatorial Pd–S distances are, on average, 0.07 Å longer than those in the experimentally determined structure of  $[\text{Pd}([\text{18}] \text{aneS}_6)]^{3+}$  in  $[\text{Pd}([\text{18}] \text{aneS}_6)](\text{ClO}_4)_6 \cdot (\text{H}_5\text{O}_2)_3$  and the axial Pd–S distances are overestimated by an average of 0.10 Å. The S–Pd–S bond angles in  $[\text{Pd}([\text{18}] \text{aneS}_6)]^{3+}$  differ by about 2.9° from their counterparts in the experimental structure. Thus, the DFT calculations reproduce the principal structural features of  $[\text{Pd}([\text{9}] \text{aneS}_3)_2]^{3+}$  and  $[\text{Pd}([\text{18}] \text{aneS}_6)]^{3+}$  as revealed by X-ray crystallography, notably the axial elongation perpendicular to the  $xy$  plane. These observations suggest that these DFT calculations are of sufficient quality to permit a qualitative understanding of the electronic structures of  $[\text{Pd}([\text{9}] \text{aneS}_3)_2]^{3+}$  and  $[\text{Pd}([\text{18}] \text{aneS}_6)]^{3+}$ .

The calculated SOMOs for  $[\text{Pd}([\text{9}] \text{aneS}_3)_2]^{3+}$  and  $[\text{Pd}([\text{18}] \text{aneS}_6)]^{3+}$  (Figure 9 and Table 2) are composed of 26.4 and 27.1% Pd  $4d_z^2$  character, respectively. A comparison between the experimental and calculated  $g$ -matrix components is presented in Table 2 showing deviations between the calculated and experimental  $g$ -matrix of 4, 1, and 7 ppt for  $g_{zz}$ ,  $g_{xx}$  and  $g_{yy}$ , respectively. We and others have reported similar deviations between experimental and calculated  $g$ -matrix components which are ascribed to over- and under-estimations in the contributions from the second-order spin–orbit/orbital term in the calculated  $g$ -matrix.<sup>21,30,34–37</sup> Taken together the calculations reveal SOMOs in  $[\text{Pd}([\text{9}] \text{aneS}_3)_2]^{3+}$  and  $[\text{Pd}([\text{18}] \text{aneS}_6)]^{3+}$  with about 26–27% metal character, consistent with the LCAO  $a^2$  coefficients (20.4–25.0%) calculated from the spin Hamiltonian parameters derived from the simulation of the EPR spectra, and a significant contribution from the S donors of the macrocyclic ligand.

The DFT calculations on models of  $[\text{Pd}([\text{9}] \text{aneS}_3)_2]^{3+}$  and  $[\text{Pd}([\text{18}] \text{aneS}_6)]^{3+}$  identify four H atoms, associated with the ligand backbone, as the only protons that possess significant spin density (Figure 9). This observation lends support to the assignment of the superhyperfine observed in the  $g_{zz}$  region of

**Table 2.** Experimental and Calculated  $g$ -Matrix Components for  $[\text{Pd}([\text{9}] \text{aneS}_3)_2]^{3+}$  and  $[\text{Pd}([\text{18}] \text{aneS}_6)]^{3+}$

	$[\text{Pd}([\text{9}] \text{aneS}_3)_2]^{3+}$		$[\text{Pd}([\text{18}] \text{aneS}_6)]^{3+}$	
	experimental (EPR)	BP-TZP all electron	experimental (EPR)	BP-TZP all electron
$g_{zz}$	2.004	2.004	1.998	2.002
$g_{xx}$	2.048	2.049	2.048	2.047
$g_{yy}$	2.046	2.038	2.036	2.035
$\Delta g_{zz}$	2	2	–4	0
$\Delta g_{xx}$	46	47	46	45
$\Delta g_{yy}$	44	36	34	33
$\alpha^2$ /%	20.4		25.0	
SOMO composition		26.4% Pd $4d_z^2$ 47.7% S1 3p 15.7% S4 and S7 3p		27.1% Pd $4d_z^2$ 46.1% S1 3p 15.2% S4 and S7 3p

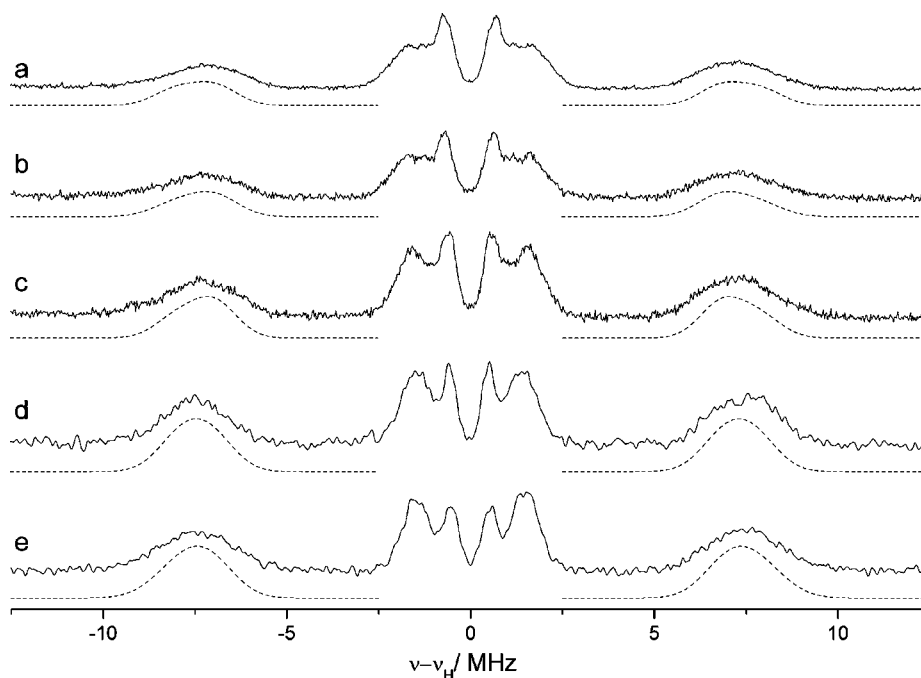


**Figure 10.** X-band Davies ENDOR spectra (20 K, DClO<sub>4</sub>) of [Pd([9]aneS<sub>3</sub>)<sub>2</sub>]<sup>3+</sup> recorded at the field positions corresponding to (a) 3432, (b) 3440, (c) 3455, (d) 3492, and (e) 3502 G. The spectra were obtained using the pulse sequence  $\pi$ -T- $\pi/2$ - $\tau$ - $\pi$ - $\tau$ -echo with mw (mw = microwave) pulse lengths of  $\pi = 256$  ns,  $\pi/2 = 128$  ns and an interpulse time  $\tau$  of 800 ns. An rf  $\pi$  pulse of variable frequency and confirm a length of 18  $\mu$ s was applied during time T of 20  $\mu$ s. The corresponding simulations are shown as dashed lines.

the frozen EPR spectra of [Pd([9]aneS<sub>3</sub>)<sub>2</sub>]<sup>3+</sup> and [Pd([18]-aneS<sub>6</sub>)]<sup>3+</sup> (Figures 5 and 7) to coupling to four protons [H2b and H9a and their symmetry-related counterparts, Figure 9] in each complex.

**Investigation of the <sup>1</sup>H Superhyperfine of [Pd([9]-aneS<sub>3</sub>)<sub>2</sub>]<sup>3+</sup> using Davies ENDOR.** Theoretical DFT calculations identified four proton atoms of the macrocyclic backbone of the ligand which lead to the superhyperfine coupling observed in the  $g_{zz}$  region of the X- and L-band frozen solution EPR spectra of [Pd([9]aneS<sub>3</sub>)<sub>2</sub>]<sup>3+</sup>. To provide further spectroscopic support for this assignment and to provide further insight into this superhyperfine coupling, [Pd([9]-aneS<sub>3</sub>)<sub>2</sub>]<sup>3+</sup> was studied using pulsed EPR and Davies ENDOR spectroscopies. The field swept echo-detected (FSED) EPR spectrum (20 K, DClO<sub>4</sub>) and the associated simulation are shown in Supporting Information, Figure SI3. The spectrum was simulated using the experimental spin Hamiltonian parameters obtained earlier by CW-EPR. No additional resolution was observed in the FSED EPR spectrum. The orientation-selective Davies ENDOR spectra are shown in Figure 10. The field positions used for these ENDOR measurements are highlighted in Supporting Information, Figure SI3.

Several small couplings (<4 MHz) were observed centered around the proton nuclear Larmor frequency ( $\nu_n$ ) at each field position. No attempt has been made to extract the spin Hamiltonian parameters for these peaks as the magnitude of the coupling implies that the protons responsible for these signals are remote from the metal center. Of greater interest are the much larger dipolar couplings (~14–16 MHz), which must arise from hydrogen atoms possessing a high electron spin density or which are close to the Pd center. An examination of Pd...<sup>1</sup>H distances (Table 3) show that protons labeled H2b and H9a (Figure 9), identified as possessing the greatest spin density from the DFT calculations, are located about 4.2 Å

**Table 3. Pd–HX Distances (Å) in [Pd([9]aneS<sub>3</sub>)<sub>2</sub>]<sup>3+</sup> with the Longest Distances Highlighted in bold**

Pd(III)–HX	distance / Å
H2b	4.2328(3)
H2c	3.7453(2)
H3b	4.1253(4)
H3c	3.3566(3)
H5b	4.1767(3)
H5c	3.6772(3)
H6b	4.1300(4)
H6c	3.3857(3)
H8a	4.1848(3)
H8B	3.7301(3)
<b>H9a</b>	<b>4.2235(4)</b>
H9b	3.5126(3)

from the Pd center. The absence of coupling from protons that are closer to the Pd center must result from the low spin densities associated with these protons. Satisfactory simulation of the Davies ENDOR spectra of [Pd([9]aneS<sub>3</sub>)<sub>2</sub>]<sup>3+</sup> was achieved by using two independent sets of spin Hamiltonian parameters indicating that there are two sets of protons responsible for the superhyperfine coupling observed in the  $g_{zz}$  regions of the frozen solution X- and L-band EPR spectra of [Pd([9]aneS<sub>3</sub>)<sub>2</sub>]<sup>3+</sup>. The spectra were satisfactorily simulated at all field positions using the hyperfine values listed in Table 4. These parameters compare well with the original estimates from the CW-EPR spectra of  $|a_{xx}({}^1\text{H})| = 4 \times 10^{-4} \text{ cm}^{-1}$ ,  $|a_{yy}({}^1\text{H})| = 5 \times 10^{-4} \text{ cm}^{-1}$ ,  $|a_{zz}({}^1\text{H})| = 5.5 \times 10^{-4} \text{ cm}^{-1}$ .

The principal values of hyperfine tensors that describe the coupling of the two sets of two protons to the electron spin are very similar (Table 4). The lower resolution of the CW X- and L-band EPR experiments were unable to distinguish between these two sets of protons, and this difference has only been

Table 4.  $^1\text{H}$  Principal Hyperfine Values for  $[\text{Pd}([\text{9}]\text{aneS}_3)_2]^{3+}$  Extracted by Simulation of the Davies ENDOR Spectra

proton	$^aA_x/\text{MHz}$	$A_y/\text{MHz}$	$A_z/\text{MHz}$	$a_{\text{iso}}/\text{MHz}$	$^b\theta_{\text{H}}/\text{deg}$	$^c\text{dist}/\text{\AA}$	UPE spin density
$^1\text{H}$ Set (a)	16.0 ( $5.3 \times 10^{-4}$ )	15.5 ( $5.1 \times 10^{-4}$ )	16.0 ( $5.3 \times 10^{-4}$ )	15.8	17	4.22	0.0056
$^1\text{H}$ Set (b)	13.5 ( $4.5 \times 10^{-4}$ )	14.0 ( $4.7 \times 10^{-4}$ )	14.0 ( $4.7 \times 10^{-4}$ )	13.8	17	4.23	0.0051

$^aA$  values are  $\pm 0.1$  MHz ( $A$  values in brackets given in  $\text{cm}^{-1}$ ).  $^b\theta_{\text{H}}$  is defined as the angle between  $g_{zz}$  and  $^{\text{H}}A_z$  ( $\pm 5^\circ$ ).  $^c\text{dist}$  are the Pd... $^1\text{H}$  distance, estimated from the dipolar component of the hyperfine interaction using the simple point dipole approximation; UPE refers to the unpaired electron spin density (or percentage 1s orbital character) at  $^1\text{H}$ .

revealed by ENDOR spectroscopy. It is not possible to make a definite assignment of the protons responsible for the peaks in the ENDOR spectra from the ENDOR simulations alone. The appreciable isotropic contribution to the hyperfine coupling for  $[\text{Pd}([\text{9}]\text{aneS}_3)_2]^{3+}$  ( $a_{\text{iso}} \sim 13.8$  or  $15.8$  MHz) indicates that the coupling arises from a strong “through-bond” interaction as a result of a large spin density on the protons, arising from their position in relation to the alignment of orbitals along the  $z$  axis. From the DFT calculations, the largest spin density was located on the two protons labeled H9a, and H2b (Figure 9) with associated Pd... $^1\text{H}$  distances given in Table 3. The experimental electron spin densities at the  $^1\text{H}$  and associated Pd... $^1\text{H}$  distances (extracted from the dipolar component of the hyperfine couplings) are given in Table 4; these values are in very good agreement with the DFT derived values, suggesting H9a and H2b are the likely candidates responsible for the observed ENDOR couplings.

## CONCLUSIONS

The electrochemical (MeCN, 0.2 M  $\text{NBu}_4\text{PF}_6$ ) or chemical oxidation (70%  $\text{HClO}_4$ ) of  $[\text{Pd}([\text{9}]\text{aneS}_3)_2](\text{PF}_6)_2$  and chemical oxidation (70%  $\text{HClO}_4$ ) of  $[\text{Pd}([\text{18}]\text{aneS}_6)](\text{PF}_6)_2$  generate paramagnetic mononuclear Pd(III) species. Single crystal X-ray crystallographic studies of  $[\text{Pd}([\text{9}]\text{aneS}_3)_2](\text{ClO}_4)_6 \cdot (\text{H}_3\text{O})_3 \cdot (\text{H}_2\text{O})_4$  and  $[\text{Pd}([\text{18}]\text{aneS}_6)](\text{ClO}_4)_6 \cdot (\text{H}_5\text{O}_2)_3$  show that  $[\text{Pd}([\text{9}]\text{aneS}_3)_2]^{3+}$  and  $[\text{Pd}([\text{18}]\text{aneS}_6)]^{3+}$  possess distorted octahedral geometries with elongated axial Pd–S interactions consistent with a formal  $4d^7$  Pd(III) center subject to a Jahn–Teller distortion. Variable temperature multifrequency CW-EPR spectroscopic studies and DFT calculations of  $[\text{Pd}([\text{9}]\text{aneS}_3)_2]^{3+}$  and  $[\text{Pd}([\text{18}]\text{aneS}_6)]^{3+}$  confirm that each cation possesses a similar SOMO that is about 26–27% Pd  $4d_z^2$  in character. This compares with the analogous group 10 complexes  $[\text{Ni}([\text{9}]\text{aneS}_3)_2]^{3+}$  and  $[\text{Pt}([\text{9}]\text{aneS}_3)_2]^{3+}$  which show about 37% Ni  $3d_z^2$  and about 30% Pt  $5d_z^2$  character, respectively. Davies ENDOR spectroscopic measurements support the assignment of super-hyperfine in the  $g_{zz}$  region of the EPR spectra of  $[\text{Pd}([\text{9}]\text{aneS}_3)_2]^{3+}$  to through-bond couplings to the Pd center involving four protons of the macrocyclic ring.

## EXPERIMENTAL SECTION

**Chemicals.** Unless otherwise stated, commercial grade chemicals were used without further purification. 1,4,7-Trithiacyclononane ( $[\text{9}]\text{aneS}_3$ ), 1,4,7,10,13,16-hexathiacyclooctadecane ( $[\text{18}]\text{aneS}_6$ ),  $[\text{Pd}([\text{9}]\text{aneS}_3)_2](\text{PF}_6)_2$ , and  $[\text{Pd}([\text{18}]\text{aneS}_6)](\text{PF}_6)_2$  were prepared according to previously reported procedures<sup>17,22,23</sup> and oxidized to their Pd(III) analogues as solutions in 70%  $\text{HClO}_4$ .

**Caution!** Perchlorate salts may be explosive when heated or ground.

**Physical Measurements.** Infrared spectra were recorded with a Nicolet Avatar 360 FT-IR spectrometer. UV/vis spectra were recorded using a Perkin-Elmer Lambda 16 spectrophotometer. Electron spray ionization (ESI) mass spectra were run on a Micromass Autospec.

Elemental analyses were carried out by the Microanalytical Service at the University of Nottingham with an Exeter Analytical Inc. CE-440 Elemental analyzer. Cyclic voltammetric and coulometric studies were carried out on an Autolab PGSTAT20 potentiostat. MeCN was freshly distilled under an atmosphere of  $\text{N}_2$  from  $\text{CaH}_2$ , and  $[\text{NBu}_4][\text{PF}_6]$  (Fluka, Electrochemical grade) was dried before use. Cyclic voltammetry was carried out on  $10^{-3}$  M solutions of the complexes under an atmosphere of Ar using Schlenk techniques. A single compartment cell was used with glassy-carbon, Pt wire, and saturated calomel functioning as working electrode, counter electrode, and reference electrode, respectively. All potentials discussed are quoted versus the ferrocene-ferrocenium couple. Coulometry was conducted in a two-compartment cell using a Pt/Rh gauze basket working electrode separated from the wound Pt/Rh gauze secondary electrode by a glass frit. UV/vis spectroelectrochemical experiments were carried out under potential control by a Sycopel Scientific Ltd. DD10 M potentiostat using a Pt/Rh gauze as a working electrode in an optically transparent electrochemical (OTE) cell (0.5 mm).

X-band EPR spectroscopic measurements of electrochemically generated samples were recorded as fluid solutions using a flat cell at room temperature (293 K) or 233 K or as frozen solutions utilizing a finger dewar filled with liquid nitrogen at 77 K using a Bruker EMX spectrometer equipped with an X-band ER041XG microwave bridge at the University of Nottingham.

Multifrequency variable-temperature EPR spectroscopic measurements were carried out at the EPSRC EPR National Service Centre in the School of Chemistry at the University of Manchester. L-band and S-band spectra were recorded using Bruker EMX/Elexsys E500 spectrometers equipped with an L-band ER065LR microwave bridge and an S-band ER061ST microwave bridge. X-band fluid spectra were collected using a Bruker EMX spectrometer equipped with an X-band ‘Super-X’ ER049X microwave bridge. Frozen X-band spectra were also recorded using this setup, but spectra were also recorded using a Bruker EMX Micro-X spectrometer equipped with an X-band ‘premium-X’ microwave bridge. Simulations of fluid EPR spectra were performed using the SimFonia<sup>38</sup> package, and all other spectra were analyzed using the EasySpin<sup>39</sup> Matlab Toolbox.

Pulsed EPR and Davies ENDOR measurements were recorded on a Bruker E580 Elexsys operating at X-band (microwave frequency  $\sim 9.73$  GHz) in the School of Chemistry at Cardiff University. The field swept echo-detected EPR (FSED EPR) was recorded at 10 K using the pulse sequence  $\pi/2 - \tau - \pi - \tau - \text{echo}$ , with a  $\pi/2_{\text{MW}}$  value of 16 ns and a  $\tau$  value of 400 ns. Davies ENDOR experiments (20 K) were carried out using the following pulse sequence:  $\pi - T - \pi/2 - \tau - \pi - \tau - \text{echo}$  with mw pulse lengths of  $\pi = 256$  ns,  $\pi/2 = 128$  ns, and an interpulse time  $\tau$  of 800 ns. An rf  $\pi$  pulse of variable frequency and a length of 18  $\mu\text{s}$  was applied during time  $T$  of 20  $\mu\text{s}$ . Spectral simulations of the ENDOR data were performed using the EasySpin<sup>39</sup> Matlab Toolbox.

DFT calculations were performed using the Amsterdam Density Functional (ADF) suite version 2010.01.<sup>40,41</sup> The unrestricted DFT calculations employed a Slater type orbital (STO) all-electron triple- $\zeta$ -plus one polarization function basis set from the ZORA/TZP database of the ADF suite for all atoms. Scalar relativistic (SR) and spin-orbit coupling (SO) approaches were used within the ZORA Hamiltonian for the inclusion of relativistic effects. The local density approximation (LDA) with the correlation potential due to Vosko et al.<sup>42</sup> was used in all of the DFT calculations. Gradient corrections were performed using the functionals of Becke<sup>43</sup> and Perdew<sup>44</sup> (BP). Models of  $[\text{Pd}([\text{9}]$

**Table 5. Crystal Data for [Pd([9]aneS<sub>3</sub>)<sub>2</sub>](PF<sub>6</sub>)<sub>2</sub>·2MeCN (1), [Pd([18]aneS<sub>6</sub>)](PF<sub>6</sub>)<sub>2</sub> (2), [Pd([9]aneS<sub>3</sub>)<sub>2</sub>](ClO<sub>4</sub>)<sub>6</sub>·(H<sub>3</sub>O)<sub>3</sub>·(H<sub>2</sub>O)<sub>4</sub> (3), and [Pd([18]aneS<sub>6</sub>)](ClO<sub>4</sub>)<sub>6</sub>·(H<sub>5</sub>O<sub>2</sub>)<sub>3</sub> (4)**

	1	2	3	4
chemical formula	C <sub>16</sub> H <sub>30</sub> S <sub>6</sub> N <sub>2</sub> P <sub>2</sub> F <sub>12</sub> Pd	C <sub>12</sub> H <sub>24</sub> S <sub>6</sub> P <sub>2</sub> F <sub>12</sub> S <sub>6</sub> Pd	C <sub>12</sub> H <sub>35</sub> S <sub>6</sub> Cl <sub>6</sub> O <sub>28</sub> Pd	C <sub>12</sub> H <sub>39</sub> S <sub>6</sub> Cl <sub>6</sub> O <sub>30</sub> Pd
<i>M</i>	839.12	757.07	1138.86	1174.89
crystal system	orthorhombic	monoclinic	monoclinic	monoclinic
space group	<i>Pccn</i>	<i>C2/m</i>	<i>P2<sub>1</sub>/c</i>	<i>P2<sub>1</sub>/c</i>
<i>a</i> /Å	11.9383(12)	19.613(4)	10.5602(11)	9.9805(2)
<i>b</i> /Å	21.693(2)	10.861(3)	9.1932(10)	10.62075(17)
<i>c</i> /Å	11.3849(11)	5.7978(12)	19.079(2)	18.2038(4)
<i>α</i> /deg	90	90	90	90
<i>β</i> /deg	90	92.922(16)	93.787(2)	99.840(2)
<i>γ</i> /deg	90	90	90	90
<i>V</i> /Å <sup>3</sup>	2948.5(5)	1233.4(5)	1848.1(3)	1901.22(6)
<i>Z</i>	4	2	2	2
<i>T</i> /K	150(2)	295(2)	150(2)	90(2)
unique data	3129	1137	3517	3711
observed data [ <i>F</i> ≥ 4σ( <i>F</i> )]	3423	913	4205	3791
refined parameters	220	83	259	278
<i>R</i> <sub>1</sub> , <i>wR</i> <sub>2</sub> [ <i>F</i> ≥ 4σ( <i>F</i> )]	0.0431, 0.1062	0.0536, 0.0649	0.0348, 0.0758	0.0322, 0.0860
<i>R</i> <sub>1</sub> , <i>wR</i> <sub>2</sub> (all data)	0.0469, 0.1089		0.0467, 0.0805	0.0331, 0.0865

aneS<sub>3</sub>)<sub>2</sub>]<sup>3+</sup> and [Pd([18]aneS<sub>6</sub>)]<sup>3+</sup> in *C<sub>i</sub>* symmetry were constructed using geometrical data from the X-ray crystal structures of the complexes. The coordinate frames employed in the calculations are shown in Figure 8 with the *x* and *y* axes bisecting the S4–Pd–S7 angles for both [Pd([9]aneS<sub>3</sub>)<sub>2</sub>]<sup>3+</sup> and [Pd([18]aneS<sub>6</sub>)]<sup>3+</sup>. For each model the *x* and *y* axes lie in the equatorial plane. The model geometries were optimized at the ZORA SR level. The *g*-matrix for each complex was obtained from an unrestricted ZORA SO calculation using the collinear approximation on the geometry optimized structure derived from the unrestricted ZORA SR calculation.

**Synthesis.** [Pd([9]aneS<sub>3</sub>)<sub>2</sub>](PF<sub>6</sub>)<sub>2</sub>·2MeCN (24 mg, 0.14 mmol) was reacted with [9]aneS<sub>3</sub> (48.9 mg, 0.28 mmol) in H<sub>2</sub>O/MeOH (1:1 v/v, 30 mL) by heating to reflux for 0.5 h. To the resulting blue solution, NH<sub>4</sub>PF<sub>6</sub> was added in excess, and the solution cooled to precipitate blue-green microcrystals. The product was collected, dissolved in CH<sub>3</sub>CN, and diffused with Et<sub>2</sub>O to yield [Pd([9]aneS<sub>3</sub>)<sub>2</sub>](PF<sub>6</sub>)<sub>2</sub>·2MeCN as dark blue blocky crystals. Yield 184 mg, 87%. Anal. Calcd for C<sub>12</sub>H<sub>24</sub>S<sub>6</sub>P<sub>2</sub>F<sub>12</sub>Pd: Expected: C, 19.07; H, 3.17. Found: C, 19.00; H, 3.16. IR (KBr, cm<sup>-1</sup>): 3672 (s), 3406 (vs), 2966 (s), 1443 (s), 1410 (s), 1287 (s), 847 (vs) 558 (vs). M.S. (ESI): *m/z* 465 for [M – H] – (PF<sub>6</sub>)<sub>2</sub><sup>+</sup> with correct isotopic distribution. UV/vis (in CH<sub>3</sub>CN) [λ<sub>max</sub> = 619 nm (ε<sub>max</sub> = 56 L mol<sup>-1</sup> cm<sup>-1</sup>)] broad, 294 (15000). Blue block crystals suitable for X-ray crystallographic analysis were grown by diffusion of Et<sub>2</sub>O vapor into a MeCN solution of the complex.

[Pd([9]aneS<sub>3</sub>)<sub>2</sub>](ClO<sub>4</sub>)<sub>6</sub>·(H<sub>3</sub>O)<sub>3</sub>·(H<sub>2</sub>O)<sub>4</sub>. The Pd(II) complex [Pd([9]aneS<sub>3</sub>)<sub>2</sub>](PF<sub>6</sub>)<sub>2</sub> was dissolved in HClO<sub>4</sub> (70% redistilled, 99.999% metals basis) (ca. 1 mL) and was stored at –20 °C for 1 week after which time dark red tabular crystals suitable for X-ray crystallographic analysis deposited.

[Pd([18]aneS<sub>6</sub>)](PF<sub>6</sub>)<sub>2</sub>. PdCl<sub>2</sub> (15 mg, 0.08 mmol) was reacted with [18]aneS<sub>6</sub> (61 mg, 0.17 mmol) in H<sub>2</sub>O/MeOH (1:1 v/v, 25 mL) by heating to reflux for 2 h. To the resulting green-brown solution, NH<sub>4</sub>PF<sub>6</sub> was added in excess and the solution cooled to precipitate a green solid. Yield 72 mg, 56%. Anal. Calcd for C<sub>12</sub>H<sub>24</sub>S<sub>6</sub>P<sub>2</sub>F<sub>12</sub>Pd: C, 19.07; H, 3.17. Found: C, 19.06; H, 3.03; IR (KBr, cm<sup>-1</sup>): 2980 (s), 2950 (s), 1430 (s), 1287 (s), 1250 (m), 1185 (m), 1151 (m), 1115 (vs), 1010 (vs). M.S. (ESI): *m/z* 466 for [M – (PF<sub>6</sub>)<sub>2</sub>]<sup>+</sup> with correct isotopic distribution.

[Pd([18]aneS<sub>6</sub>)](ClO<sub>4</sub>)<sub>6</sub>·3(H<sub>5</sub>O<sub>2</sub>). The Pd(II) complex [Pd([18]aneS<sub>6</sub>)](PF<sub>6</sub>)<sub>2</sub> was dissolved in HClO<sub>4</sub> (70% redistilled, 99.999% metals basis) (ca. 1 mL) and was stored at –20 °C for 1 week after which time dark red blocky crystals suitable for X-ray crystallographic analysis deposited.

**X-ray Crystallography.** Single crystal X-ray diffraction data for [Pd([9]aneS<sub>3</sub>)<sub>2</sub>](PF<sub>6</sub>)<sub>2</sub>·2MeCN and [Pd([9]aneS<sub>3</sub>)<sub>2</sub>]-

(ClO<sub>4</sub>)<sub>6</sub>·(H<sub>3</sub>O)<sub>3</sub>·(H<sub>2</sub>O)<sub>4</sub> were collected using a Bruker SMART APEX CCD area detector diffractometer equipped with an Oxford Cryosystems low-temperature device. Reflection data were collected with Mo-*K*<sub>α</sub> X-radiation (λ = 0.71073 Å) at 150 K. Single crystals were coated in a film of perfluoropolyether (Lancaster Synthesis Fomblin YR-1800) and mounted on dual-stage glass fibers for X-ray diffraction studies and cooled using dry ice during transfer to the diffractometer. Single crystal X-ray diffraction data for [Pd([18]aneS<sub>6</sub>)]-(ClO<sub>4</sub>)<sub>6</sub>·(H<sub>3</sub>O)<sub>3</sub> were collected using an Oxford Diffraction Supernova single source diffractometer, equipped with an Atlas CCD detector and an Oxford Cryosystems low-temperature device using Cu-*K*<sub>α</sub> X-radiation (λ = 1.54184 Å) at 90 K. A single crystal was coated in a film of perfluoropolyether (Lancaster Synthesis Fomblin YR-1800) and mounted on a MicroMount (MiTeGen). A dark green crystal of [Pd([18]aneS<sub>6</sub>)](PF<sub>6</sub>)<sub>2</sub> was mounted to rotate about its crystallographic *c*-axis on a Stoe Stadi-2 two-circle diffractometer, and data were collected as ω scans at ambient temperature using Mo-*K*<sub>α</sub> X-radiation (λ = 0.71073 Å). Structures were solved by direct methods using the SHELXTL<sup>45</sup> suite of programs, and apart from disordered fluorine atoms of one of the hexafluorophosphate anions in [Pd([9]aneS<sub>3</sub>)<sub>2</sub>](PF<sub>6</sub>)<sub>2</sub>·2MeCN and the unique, disordered C atom in [Pd([18]aneS<sub>6</sub>)](PF<sub>6</sub>)<sub>2</sub>, all non-hydrogen atoms were refined using anisotropic displacement parameters, as were the statistically disordered H atoms on the dihydronium cations in [Pd([18]aneS<sub>6</sub>)]-(ClO<sub>4</sub>)<sub>6</sub>·(H<sub>5</sub>O<sub>2</sub>)<sub>3</sub> and the disordered H<sub>3</sub>O<sup>+</sup> cations in [Pd([9]aneS<sub>3</sub>)<sub>2</sub>](ClO<sub>4</sub>)<sub>6</sub>·(H<sub>3</sub>O)<sub>3</sub>·(H<sub>2</sub>O)<sub>4</sub>. For [Pd([18]aneS<sub>6</sub>)]-(ClO<sub>4</sub>)<sub>6</sub>·(H<sub>5</sub>O<sub>2</sub>)<sub>3</sub> H atoms were geometrically placed resulting in a statistical disorder of the bridging hydrogen atoms of the dihydronium cations. This required no further intervention. For [Pd([9]aneS<sub>3</sub>)<sub>2</sub>](ClO<sub>4</sub>)<sub>6</sub>·(H<sub>3</sub>O)<sub>3</sub>·(H<sub>2</sub>O)<sub>4</sub> refinement of the crystal structure gave no problems for the [Pd([9]aneS<sub>3</sub>)<sub>2</sub>]<sup>3+</sup> cation or for the six associated ClO<sub>4</sub><sup>-</sup> anions, but a charge balance issue arose from H atom placement on O13 and O14. Contoured difference maps showed electron density associated with both which could be correlated with maxima in the list of difference electron density peaks, giving the possibility of them being H<sub>2</sub>O molecules or H<sub>3</sub>O<sup>+</sup> cations. Three well-defined electron density distributions in a sensible arrangement around O13 made it a good candidate for H<sub>3</sub>O<sup>+</sup>. For O14, one of the associated electron distributions showed some overlap with its symmetry-generated equivalent. Placing two H atoms on O14 left two remaining difference peaks, of which one had more reasonable geometry than the other. The third H atom on O14 (H14C) was associated with a significantly lower difference peak. The crystal structure was refined with both full and half occupancy on all H atoms and the resulting discrepancy analysis examined to test each model. A free variable was introduced to

allow the refinement of the H atom occupancies, taking into account that by symmetry H14C could never be more than half-occupied. The best model was one where O14 was 50:50 H<sub>2</sub>O/H<sub>3</sub>O<sup>+</sup>, making the overall stoichiometry Pd([9]aneS<sub>3</sub>)<sub>2</sub><sup>3+</sup>·6(ClO<sub>4</sub><sup>-</sup>)·3(H<sub>3</sub>O<sup>+</sup>)·4H<sub>2</sub>O. In Pd([18]aneS<sub>6</sub>)(PF<sub>6</sub>), the asymmetric unit comprises one-quarter of a cation and one-half of an anion: Pd1 resides on site of 2/m symmetry, S1 and S10 both lie on a mirror plane. Atom C5 is disordered over two half-occupied sites. In the anion, P1, F1, and F2 lie on a mirror plane. Crystal data and refinement details are given in Table 5. CCDC 836800–836802 contain the supplementary crystallographic data for this paper. These data can be obtained free of charge from the Cambridge Crystallographic Data Centre via [www.ccdc.cam.ac.uk/data\\_request/cif](http://www.ccdc.cam.ac.uk/data_request/cif).

## ■ ASSOCIATED CONTENT

### ■ Supporting Information

Crystallographic data in CIF format. Further details are given in Figures S11–S13 and Tables S11–S12. This material is available free of charge via the Internet at <http://pubs.acs.org>.

## ■ AUTHOR INFORMATION

### Corresponding Author

\*E-mail: M.Schroder@nottingham.ac.uk (M.S.), J.McMaster@nottingham.ac.uk (J.M.).

## ■ ACKNOWLEDGMENTS

We thank the EPSRC and the University of Nottingham for support and funding. M.S. gratefully acknowledges receipt of a Royal Society Wolfson Merit Award and of an ERC Advanced Grant. We acknowledge use of the EPSRC U.K. National Electron Paramagnetic Resonance Service at The University of Manchester.

## ■ REFERENCES

- (1) Powers, D. C.; Ritter, T. *Top. Organomet. Chem.* **2011**, *35*, 129.
- (2) Cotton, F. A.; Gu, J.; Murillo, C. A.; Timmons, D. J. *J. Am. Chem. Soc.* **1998**, *120*, 13280.
- (3) Chuang, G. J.; Wang, W.; Lee, E.; Ritter, T. *J. Am. Chem. Soc.* **2011**, *133*, 1760.
- (4) Cotton, F. A.; Koshevoy, I. O.; Lahuerta, P.; Murillo, C. A.; Sanau, M.; Ubeda, M. A.; Zhao, Q. *J. Am. Chem. Soc.* **2006**, *128*, 13674.
- (5) Powers, D. C.; Benitez, D.; Tkatchouk, E.; Goddard, W. A. III; Ritter, T. *J. Am. Chem. Soc.* **2010**, *132*, 14092.
- (6) Powers, D. C.; Ritter, T. *Nat. Chem.* **2009**, *1*, 302.
- (7) (a) Khusnutdinova, J. R.; Rath, N. P.; Mirica, L. M. *Angew. Chem., Int. Ed.* **2011**, *50*, 5532. (b) Yamashita, M.; Takaishi, S. *Chem. Commun.* **2010**, *46*, 4438.
- (8) Khusnutdinova, J. R.; Rath, N. P.; Mirica, L. M. *J. Am. Chem. Soc.* **2010**, *132*, 7303.
- (9) Nyholm, R. *J. Chem. Soc.* **1952**, 3579.
- (10) Sharpe, A. *J. Chem. Soc.* **1950**, 3444.
- (11) Bartlett, N. *Proc. Chem. Soc. Lond.* **1964**, 393.
- (12) Tressaud, A. *C. R. Acad. Sci. Paris.* **1976**, *282*, 1069.
- (13) Tressaud, A. *J. Fluorine Chem.* **1982**, *21*, 28.
- (14) Tressaud, A. *Z. Anorg. Allg. Chem.* **1984**, *517*, 43.
- (15) Tressaud, A. *J. Fluorine Chem.* **1985**, *29*, 39.
- (16) McAuley, A.; Whitcombe, T. W. *Inorg. Chem.* **1988**, *27*, 3090.
- (17) (a) Blake, A. J.; Holder, A. J.; Hyde, T. I.; Schröder, M. *J. Chem. Soc., Chem. Commun.* **1987**, 987.
- (18) Blake, A. J.; Gould, R. O.; Halcrow, M. A.; Holder, A. J.; Hyde, T. I.; Schröder, M. *J. Chem. Soc., Dalton Trans.* **1992**, 3427.
- (19) (a) Blake, A. J.; Gould, R. O.; Holder, A. J.; Hyde, T. I.; Lavery, A. J.; Odulate, M. O.; Schröder, M. *J. Chem. Soc., Chem. Commun.* **1987**, 118. (b) Wiegardt, K.; Küppers, H.-J.; Raabe, E.; Krüger, C. *Angew. Chem., Int. Ed. Engl.* **1986**, *25*, 1101. (c) Blake, A. J.; Holder, A. J.; Hyde, T. I.; Roberts, Y. V.; Lavery, A. J.; Schröder, M. *J. Organomet. Chem.* **1987**, *323*, 261.
- (20) Stephen, E.; Blake, A. J.; Davies, E. S.; McMaster, J.; Schröder, M. *Chem. Commun.* **2008**, 5707.
- (21) (a) Shaw, J. L.; Wolowska, J.; Collison, D.; Howard, J. A. K.; McInnes, E. J. L.; McMaster, J.; Blake, A. J.; Wilson, C.; Schröder, M. *J. Am. Chem. Soc.* **2006**, *128*, 13827. (b) Blake, A. J.; Greig, J. A.; Holder, A. J.; Hyde, T. I.; Taylor, A.; Schröder, M. *Angew. Chem., Int. Ed. Engl.* **1990**, *29*, 197. (c) Blake, A. J.; Gould, R. O.; Greig, J. A.; Holder, A. J.; Hyde, T. I.; Schröder, M. *J. Chem. Soc., Chem. Commun.* **1989**, 876. (d) Blake, A. J.; Collison, D.; Gould, R. O.; Reid, G.; Schröder, M. *J. Chem. Soc., Dalton Trans.* **1993**, 521.
- (22) Blower, P. J.; Cooper, S. R. *Inorg. Chem.* **1987**, *26*, 2009.
- (23) Blake, A. J.; Gould, R. O.; Lavery, A. J.; Schröder, M. *Angew. Chem., Int. Ed. Engl.* **1986**, *25*, 274.
- (24) Grant, G. J.; Spangler, N. J.; Setzer, W. N.; VanDerveer, D. G.; Mehne, L. F. *Inorg. Chim. Acta* **1996**, *31*.
- (25) Blake, A. J.; Crofts, R. D.; Schröder, M. *J. Chem. Soc., Dalton Trans.* **1993**, 2259.
- (26) Grant, G. J.; Sanders, K. A.; Setzer, W. N.; vanDerveer, D. G. *Inorg. Chem.* **1991**, *30*.
- (27) (a) Blake, A. J.; Reid, G.; Schröder, M. *J. Chem. Soc., Dalton Trans.* **1990**, 3363. (b) Blake, A. J.; Gould, R. O.; Hyde, T. I.; Schröder, M. *J. Chem. Soc., Chem. Commun.* **1987**, 431.
- (28) Stephen, E.; Huang, D.; Shaw, J. L.; Blake, A. J.; Collison, D.; Davies, E. S.; Edge, R.; Howard, J. A. K.; McInnes, E. J. L.; Wilson, C.; Wolowska, J.; McMaster, J.; Schröder, M. *Chem.—Eur. J.* **2011**, *17*, 10246–10258.
- (29) Mabbs, F. E.; Collison, D. *Electronic Paramagnetic Resonance of d Transition Metal Compounds*; Elsevier Science: New York, 1992.
- (30) Huang, D.; Zhang, X.; McInnes, E. J. L.; McMaster, J.; Blake, A. J.; Davies, E. S.; Wolowska, J.; Wilson, C.; Schröder, M. *Inorg. Chem.* **2008**, *47*, 9919.
- (31) Rieger, P. H. *Coord. Chem. Rev.* **1994**, *135*, 203.
- (32) Rieger, P. H. *J. Magn. Reson.* **1997**, *124*, 140.
- (33) Huang, D.; Blake, A. J.; McInnes, E. J. L.; McMaster, J.; Davies, E. S.; Wilson, C.; Wolowska, J.; Schröder, M. *Chem. Commun.* **2008**, 1305.
- (34) Patchkovskii, S.; Ziegler, T. *J. Chem. Phys.* **1999**, *111*, 5730.
- (35) Patchkovskii, S.; Ziegler, T. *J. Am. Chem. Soc.* **2000**, *122*, 3506.
- (36) Stein, M.; van Lenthe, E.; Baerends, E. J.; Lubitz, W. *J. Phys. Chem. A* **2001**, *105*, 416.
- (37) van Lenthe, E.; van der Avoird, A.; Hagen, W. R.; Reiijerse, E. J. *J. Phys. Chem. A* **2000**, *104*, 2070.
- (38) *SimFonia*; Bruker Analytische Messtechnik GmbH, Berlin, Germany, 1996.
- (39) Stoll, S.; Schweiger, A. *J. Magn. Reson.* **2006**, *178*, 42.
- (40) Guerra, C. F.; Snijders, J. G.; te Velde, G.; Baerends, E. J. *Theor. Chem. Acc.* **1998**, *99*, 391.
- (41) Velde, G. T.; Bickelhaupt, F. M.; Baerends, E. J.; Guerra, C. F.; Van Gisbergen, S. J. A.; Snijders, J. G.; Ziegler, T. *J. Comput. Chem.* **2001**, *22*, 931.
- (42) Vosko, S. H.; Wilk, L.; Nusair, M. *Can. J. Phys.* **1980**, *58*, 1200.
- (43) Becke, A. D. *Phys. Rev. A* **1988**, *38*, 3098.
- (44) Perdew, J. P. *Phys. Rev. B* **1986**, *33*, 8822.
- (45) Sheldrick, G. M. *Acta Crystallogr., Sect A* **2008**, *64*, 112.